Cell Host & Microbe

Integrative Imaging Reveals SARS-CoV-2-Induced Reshaping of Subcellular Morphologies

Graphical Abstract
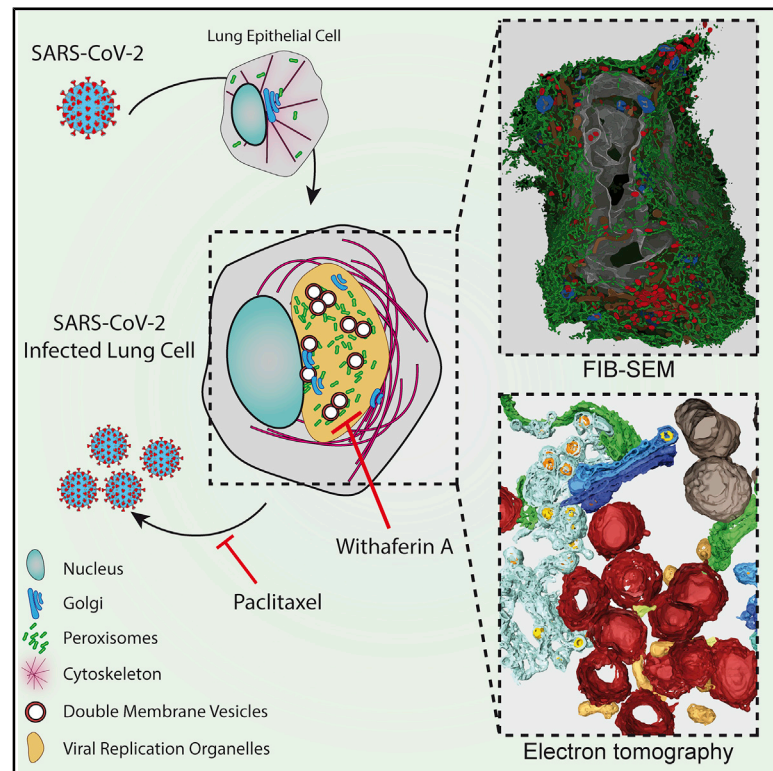
Authors

Mirko Cortese, Ji-Young Lee,
Berati Cerikan, ...,
Laurent Chatel-Chaix,
Yannick Schwab, Ralf Bartenschlager

Correspondence

mirko.cortese@med.uni-heidelberg.de
(M.C.),
yannick.schwab@embl.de (Y.S.),
ralf.bartenschlager@
med.uni-heidelberg.de (R.B.)

In Brief

Cortese et al. use integrative imaging techniques to generate a publicly available repository of morphological alterations induced by SARS-CoV-2 in lung cells. Accumulation of ER-derived double-membrane vesicles, the viral replication organelle, occurs concomitantly with cytoskeleton remodeling and Golgi fragmentation. Pharmacological alteration of cytoskeleton dynamics restricts viral replication and spread.

Highlights

- Integrative imaging approaches reveal SARS-CoV-2-induced cellular alterations

- SARS-CoV-2 extensively remodels the cellular endomembrane system

- Pharmacological inhibition of cytoskeleton remodeling restricts viral replication

- We provide a comprehensive repository of virus-induced ultrastructural cell changes

CellPress

Article

Integrative Imaging Reveals SARS-CoV-2-Induced Reshaping of Subcellular Morphologies

Mirko Cortese,[1,*] Ji-Young Lee,[1,10] Berati Cerikan,[1] Christopher J. Neufeldt,[1] Viola M.J. Oorschot,[3] Sebastian Köhrer,[2,14] Julian Hennies,[2,4] Nicole L. Schieber,[2] Paolo Ronchi,[3] Giulia Mizzon,[2,3] Inés Romero-Brey,[2] Rachel Santarella-Mellwig,[3] Martin Schorb,[3] Mandy Boermel,[3] Karel Mocaer,[2] Marianne S. Beckwith,[2] Rachel M. Templin,[2] Viktoriia Gross,[2] Constantin Pape,[5,6] Christian Tischer,[7] Jamie Frankish,[8] Natalie K. Horvat,[6,9] Vibor Laketa,[10] Megan Stanifer,[1] Steeve Boulant,[11,12] Alessia Ruggieri,[1] Laurent Chatel-Chaix,[13] Yannick Schwab,[2,3,*] and Ralf Bartenschlager[1,10,15,16,*]

[1]Department of Infectious Diseases, Molecular Virology, Heidelberg University, 69120 Heidelberg, Germany
[2]Cell Biology and Biophysics Unit, European Molecular Biology Laboratory, 69117 Heidelberg, Germany
[3]Electron Microscopy Core Facility, European Molecular Biology Laboratory, 69117 Heidelberg, Germany
[4]Collaboration for joint PhD degree between EMBL and Heidelberg University, Faculty of Biosciences, Heidelberg, Germany
[5]Interdisciplinary Center for Scientific Computing, Heidelberg University, Heidelberg, Germany
[6]European Molecular Biology Laboratory (EMBL), 69117 Heidelberg, Germany
[7]Center for Bioimage Analysis, European Molecular Biology Laboratory, Heidelberg, Germany
[8]BioMed X Institute, BioMed X GmbH, 69120 Heidelberg, Germany
[9]Molecular Medicine Partnership Unit (MMPU), Otto-Meyerhof-Zentrum, Im Neuenheimer Feld 350, 69120 Heidelberg, Germany
[10]German Center for Infection Research, Heidelberg partner site, Heidelberg, Germany
[11]Research Group "Cellular polarity and viral infection," German Cancer Research Center (DKFZ), 69120 Heidelberg, Germany
[12]Department of Infectious Diseases, Virology, Heidelberg University, 69120 Heidelberg, Germany
[13]Institut National de la Recherche Scientifique, Centre Armand-Frappier Santé Biotechnologie, 531, Boulevard des Prairies Laval, Québec, QC H7V 1B7, Canada
[14]Clinical Cooperation Unit Molecular Hematology/Oncology, German Cancer Research Center (DKFZ), 69120 Heidelberg, Germany
[15]Division Virus-Associated Carcinogenesis, German Cancer Research Center (DKFZ), 69120 Heidelberg, Germany
[16]Lead Contact
*Correspondence: mirko.cortese@med.uni-heidelberg.de (M.C.), yannick.schwab@embl.de (Y.S.), ralf.bartenschlager@med.uni-heidelberg.de (R.B.)
https://doi.org/10.1016/j.chom.2020.11.003

SUMMARY

Pathogenesis induced by SARS-CoV-2 is thought to result from both an inflammation-dominated cytokine response and virus-induced cell perturbation causing cell death. Here, we employ an integrative imaging analysis to determine morphological organelle alterations induced in SARS-CoV-2-infected human lung epithelial cells. We report 3D electron microscopy reconstructions of whole cells and subcellular compartments, revealing extensive fragmentation of the Golgi apparatus, alteration of the mitochondrial network and recruitment of peroxisomes to viral replication organelles formed by clusters of double-membrane vesicles (DMVs). These are tethered to the endoplasmic reticulum, providing insights into DMV biogenesis and spatial coordination of SARS-CoV-2 replication. Live cell imaging combined with an infection sensor reveals profound remodeling of cytoskeleton elements. Pharmacological inhibition of their dynamics suppresses SARS-CoV-2 replication. We thus report insights into virus-induced cytopathic effects and provide alongside a comprehensive publicly available repository of 3D datasets of SARS-CoV-2-infected cells for download and smooth online visualization.

INTRODUCTION

As of end of September 2020, the ongoing COVID-19 pandemic has caused almost one million fatalities and has affected more than 30 million individuals with confirmed infection worldwide (https://covid19.who.int/). A second wave of infections is occurring in many countries and the severe acute respiratory syndrome coronavirus 2 (SARS-CoV-2), the etiologic agent of this disease, is expected to become seasonal. Thus, there is an

urgent need to develop and implement both prophylactic and therapeutic strategies against this virus. Tremendous efforts are being deployed to rapidly develop a safe-guarding vaccine with no less than 150 candidates currently under evaluation. Therefore, much attention has been drawn to the study of virion structure and potential surface epitopes relevant for induction of neutralizing antibodies (Chu et al., 2020; Wrapp et al., 2020). In stark contrast, much less is known about how SARS-CoV-2 drives pathogenesis, but it is becoming clear that disease

severity is determined by two parameters. These are a predominantly inflammatory cytokine response triggered by the virus and direct cytopathogenicity of SARS-CoV-2, leading to death of infected cells by a so far poorly characterized mechanism (Chu et al., 2020; Huang et al., 2020; Tang et al., 2020). Knowledge about viral cytopathogenicity requires detailed insights into how SARS-CoV-2 replicates in and alters its host cell. Information gained in this area is expected to foster the development of innovative therapy mitigating disease severity. However, thus far such insights have been mostly inferred from studies on related betacoronaviruses such as the highly pathogenic Middle East respiratory syndrome coronavirus (MERS-CoV) and SARS-CoV-1, the mouse hepatitis virus (MHV) model system, or some endemic coronaviruses causing common cold. Although some approved drugs are considered for repurposing strategies (e.g., hydroxychloroquine or combination therapy of lopinavir-ritonavir) because of their antiviral activity in cell culture, the clinical benefit of these drugs in terms of survival outcome and severity of symptoms is disputed (Marzolini et al., 2020). Therefore, there is a need to better understand the biological mechanisms driving the SARS-CoV-2 replication cycle in order to identify therapeutic targets and develop highly efficient drugs suppressing viral replication and virus-induced cell death.

After viral entry initiated by the binding of Spike (S) viral protein to cell surface receptors, the best-studied one being angiotensin I converting enzyme 2 (ACE2), and S processing by cellular proteases (Hoffmann et al., 2020), the 30 kb-long positive-strand RNA genome is released into the cytoplasm. There, the two large open reading frames, 1a and, via ribosomal frameshifting, 1a/b are translated giving rise to the replicase (rep) polyproteins rep1a and rep1a/1b, respectively. These viral products are cleaved by viral proteases to generate 16 mature nonstructural proteins (nsps), most of them constituting the replication-transcription complex responsible for viral RNA synthesis. During replication, several sub-genomic RNA species are generated encoding for four structural proteins and multiple accessory proteins. The structural proteins membrane (M), nucleocapsid (N), envelope (E), and S, together with the genomic RNA, drive the assembly of new virus particles, which in the case of other coronaviruses bud into the endoplasmic reticulum-Golgi intermediate compartment (ERGIC). Virions are transported through the secretory pathway and are released out of the cell (Perlman and Masters, 2020).

Like all positive-strand RNA viruses (Paul and Bartenschlager, 2013), SARS-CoV-2 induces a remodeling of cellular endomembranes to form viral replication organelles (vROs). These structures are thought to create a microenvironment conducive to RNA synthesis by allowing the enrichment of metabolites, viral enzymes and cofactors, and by protecting viral RNA from degradation and sensing by pattern recognition receptors of the innate immune system. Coronavirus replication organelles (ROs) are composed predominantly of double-membrane vesicles (DMVs) that are most likely derived from the endoplasmic reticulum (ER) (Klein et al., 2020; Knoops et al., 2008; Snijder et al., 2020). The interior of these structures contains double-stranded (ds)RNA, the presumed viral replication intermediate, and *de novo* synthesized RNA, demonstrating that DMVs are the sites of viral RNA synthesis. A pore-like opening spanning the two membrane layers of DMVs has been reported very recently,

consistent with release of newly synthesized RNA from the DMV interior into the cytoplasm (Wolff et al., 2020).

Although these studies show that SARS-CoV-2 infection induces DMV formation as sites of viral RNA replication, the biogenesis of these structures and their link to subcellular compartments is poorly defined. Moreover, although SARS-CoV-2 infection is highly cytopathic, the effect of the virus on integrity and morphology of cellular organelles has not been established.

In this study, we employed a combination of light and electron microscopy approaches to obtain an integrative view of the 3D architecture of SARS-CoV-2-induced vROs, their inter-relation with subcellular compartments, and the effect of viral infection on cellular organelles. We show whole-cell 3D reconstructions demonstrating profound morphological remodeling of multiple membranous organelles such as fragmentation of the Golgi and recruitment of peroxisomes to vROs. In addition, using live cell imaging in combination with a sensor monitoring productive infection and replication, we show that DMV clusters are delimited by a reorganized "cage-like" vimentin network and that pharmacological inhibition of vimentin blocks viral replication. *In cellulo* electron tomography and focused ion beam scanning electron microscopy (FIB-SEM) data unveiled a network of interconnected DMVs that are tethered to the endoplasmic reticulum (ER) by membrane connectors, providing insights into DMV biogenesis and their role in coordinating the different steps of SARS-CoV-2 replication. Altogether, our study provides a comprehensive 3D view of the SARS-CoV-2 replication cycle and alterations of cellular organelles most likely contributing to cytopathogenicity of the virus and possibly serving as target for urgently needed therapeutic strategies.

RESULTS

Kinetics of Viral Replication Organelle Formation in SARS-CoV-2-Infected Human Pulmonary Epithelial Cells

Human pulmonary epithelial Calu-3 cells are known to be permissive to SARS-CoV-2 and therefore were used as model system to study the morphological remodeling of the cell induced by viral infection. From 6 h after infection onward, SARS-CoV-2+ cells as well as intra- and extracellular viral RNA and infectious virus released into the cell culture supernatant became detectable (Figures 1A–1E). Thus, a full replication cycle can be completed within less than 6 h in Calu-3 cells. At 12 and 24 h after infection, the number of infected cells increased up to 70% (Figure 1B), concomitant with an increase of intra- and extracellular viral RNA as well as virus titers as determined by infectivity assay (Figures 1C–1E). Ultrastructural analysis performed by transmission electron microscopy (TEM) revealed a parallel appearance of DMVs, becoming detectable as sporadic clusters of small-sized DMVs (diameter 185 nm ± 28 nm) at 6 h after infection and increasing in abundance and diameter (298 nm ± 42 nm) until 24 h after infection (Figures 1F and 1G). In some cases, large areas covered with glycogen granules, in close proximity of lipid droplets, and membranous cisternae were present within infected cells (Figure 1Fii, bottom and 1Fiii, middle). Virions assembling within the Golgi compartments as well as few extracellular virions were observed, starting at 6 h after infection and also increasing in abundance at later time points
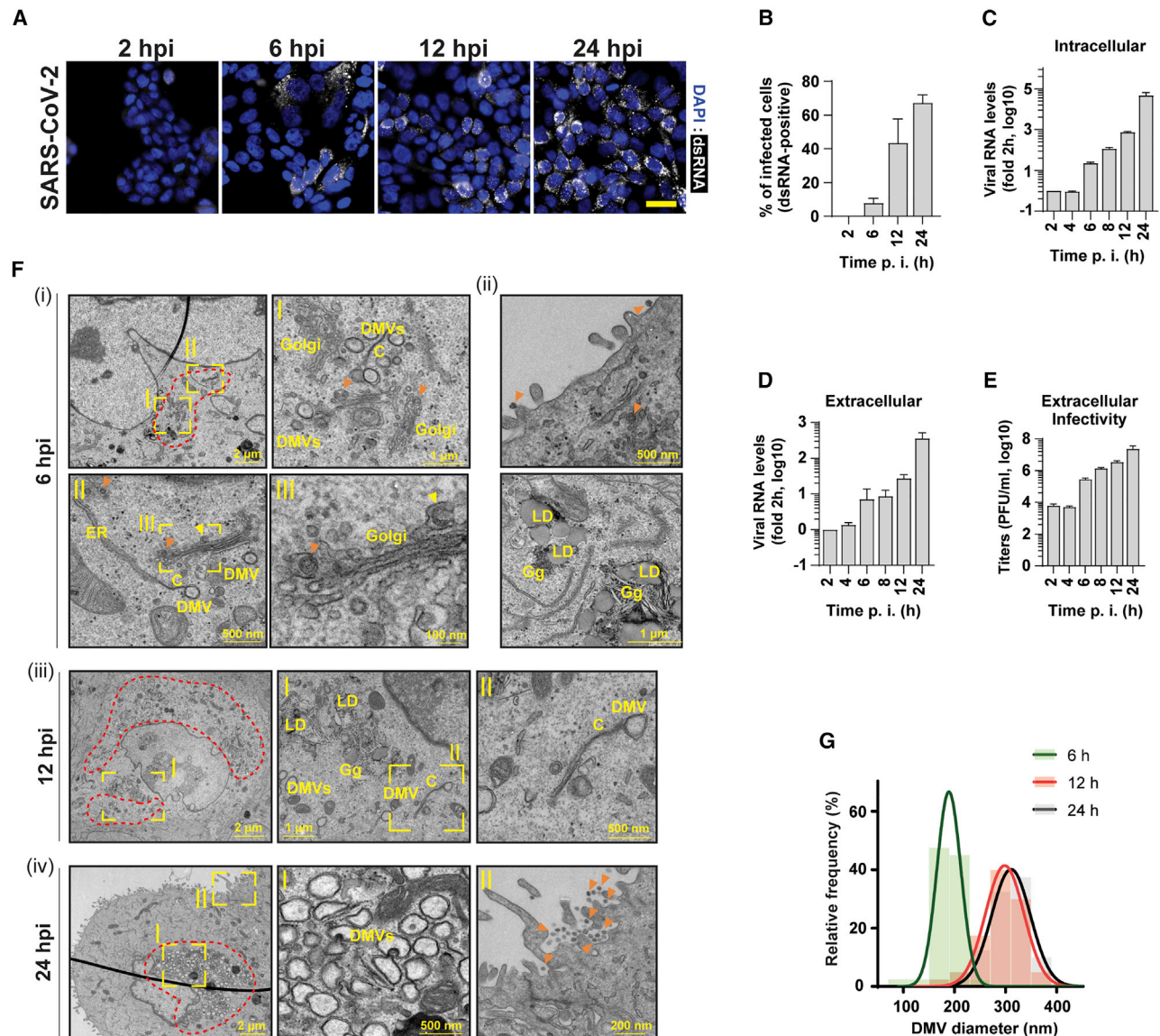
Figure 1. SARS-CoV-2 Infection Kinetics in Pulmonary Epithelial Cells

(A) Time course of SARS-CoV-2 replication in infected Calu-3 cells (multiplicity of infection [MOI] = 5) as detected by immunofluorescence using a dsRNA antibody (white). Nuclear DNA was stained with DAPI (blue). Scale bar, 40 μm.

(B) Percentage of dsRNA^{+} cells quantified from (A).

(C and D) Intra- and extracellular viral RNA levels measured by RT-qPCR.

(E) Extracellular infectivity measured by plaque assay. Means and SDs of three independent experiments are shown in (B)–(E).

(F) Transmission electron microscopy images of 70-nm-thin sections of resin-embedded Calu-3 cells infected with SARS-CoV-2 (MOI = 5) and imaged at the indicated time points after infection. Abbreviations are as follows: DMVs, double-membrane vesicles; C, connectors; LD, lipid droplet; Gg, glycogen granules. Color coding is as follows: orange arrow heads, completed virions; yellow arrowhead, budding virion. Areas in yellow rectangles are magnified in the corresponding panels marked with roman letters. Red dotted lines indicate regions with accumulations of DMVs.

(G) Relative frequency distribution of DMV diameters determined at the different time points after infection. Gaussian fits are shown as overlay. n = 43, 40, and 48 DMVs for 6 h, 12 h, and 48 h after infection, respectively.

(Figure 1Fii top and 1Fiv, right). Notably, ER tubules with collapsed luminal space were frequently observed in close proximity to DMVs (Figure 1Fiii, right). Such structures are reminiscent of the so-called "zippered ER" or "convoluted membranes" observed in cells infected with other coronaviruses (Snijder et al., 2020). In some instances, these structures appear to connect the rough ER to the DMVs (Figure 1Fi, bottom left and 1Fiii, right).

Whole-Cell Volume 3D Analysis Reveals Tight Association of DMVs with an ER-Based Network in SARS-CoV-2-Infected Cells

To obtain a global view of the cellular alterations induced by SARS-CoV-2 infection, we applied FIB-SEM analysis on infected Calu-3 cells. The full volumes of three infected cells (infection being determined by the presence of DMVs), and
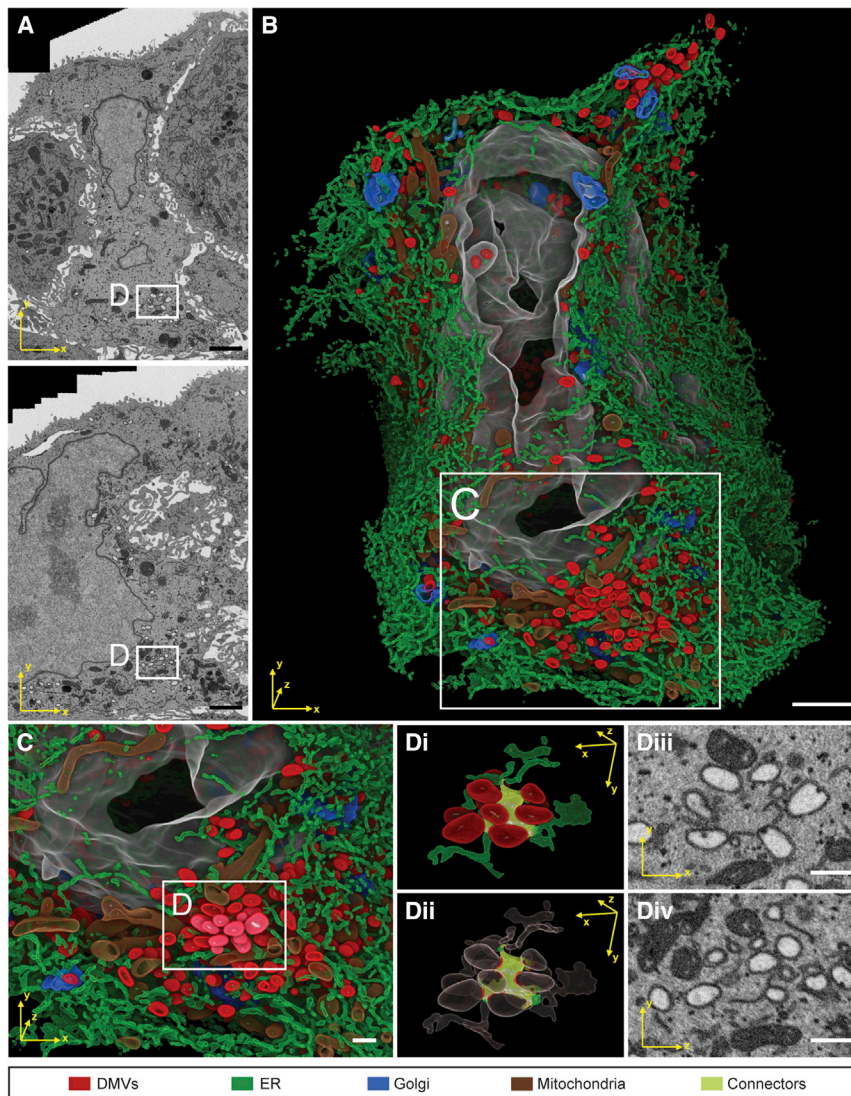
Figure 2. FIB-SEM Analysis of Whole-Cell Volume of a SARS-CoV-2-Infected Cell Reveals a Network of DMVs and ER

Calu-3 cells were infected with SARS-CoV-2 (MOI = 5) for 24 h before being fixed and prepared for FIB-SEM analysis.

(A) Two different slices through the cell volume. Note the tight association of the infected cell in the middle with the neighboring cells, giving the infected cell an hourglass-like shape, shown at the top.

(B) 3D rendering of the infected cell. The color code of subcellular structures is depicted on the bottom of the figure.

(C) Zoom-in of the area indicated with rectangle in (B) showing a cluster of DMVs.

(D) Detail of DMV-ER connections (i). DMVs are shown in red, membrane connectors are shown in citrus. (ii) is the same as in (i) but with high-level transparencies for DMVs and ER regions, except the areas in contact with the ER connectors. In (iii and iv) are two orthogonal slices showing the raw data of the same region of the respective left panel. Scale bars, 2 μm in (A) and (B); 500 nm in (C) and (D).

See also Figure S1 and Video S1.

Rendering and 3D visualization of the whole segmented dataset revealed an intricate network of DMVs embedded in an ER matrix. The majority of DMVs accumulated on the side of the cell attached to the culture substrate (Figure 2B), although groups of DMVs were present throughout the cell and always in contact with the ER network. Closer inspection showed that the ER tubules with narrow luminal space linked several DMVs together, also connecting them to the larger ER network (Figures 2C and 2D; Video S1). Therefore, we have named these structures "ER connectors."

two mock-inoculated cells that served as reference, were acquired (the complete datasets are made available for download on EMPIAR—ID 10490, and are viewable in an interactive manner via MoBIE—see STAR Methods and Table S1). Subsequently, we applied a bottom-up approach, efficiently combining semi-automated and automated segmentation based on the multicut pipeline (Beier et al., 2017) (see STAR Methods) to achieve deep-segmentation of the dataset (Figures 2 and S1; Video S1). Using this method, in which a small fraction of one dataset is employed to train a machine-learning-based approach for the recognition of defined and known organelles, we segmented the cellular elements from one infected cell and one mock cell, including the nucleus, the mitochondrial network, and ER, as well as viral elements, such as the DMVs and DMV-associated ER membranes (Figures 2B–2D and S1; Video S1). In addition, manual segmentation was applied for the Golgi apparatus in the infected cell (Figures 2B and 2C) and some instances in the mock cell where the upscaling was performed by using deep learning (Figure S1).

network (Figures 2C and 2D; Video S1). Therefore, we have named these structures "ER connectors."

3D Architecture of Viral Replication Organelles Provides Insights into DMV Biogenesis

To gain insight into the biogenesis of the DMVs, we determined their 3D architecture by high-resolution electron tomography analysis of SARS-CoV-2-infected Calu-3 cells. We processed a total of 13 tomograms from uninfected cells and 7, 85, and 153 dual-tilt tomograms of cells fixed at 6, 12, and 24 h after infection, respectively (Table S1; the complete dataset is made available for download on EMPIAR—ID 10490 and can be visualized through the MoBIE Fiji plugin; see Figure S2A and STAR Methods). For each tomogram, we identified and classified the cellular and viral structures present (Table S1). This large dataset allowed us to identify different topological compositions of the SARS-CoV-2 RO. Among all virus-induced structures, DMVs were the most abundant. The average diameter, calculated at the DMVs' equator, was 291 ± 48 nm for the 24 h time point, in agreement with the results from TEM (Figures S2B

and 1G, respectively). Smooth ER connectors were often found in close apposition to the DMVs' outer membranes (Figures 3A–3E). In some cases, DMVs were embedded into the rough ER such as the DMV outer membrane was contiguous to the ER membrane, and several DMVs were associated to the same ER branch (Figures 3F and 3G, respectively; Video S2). This interconnection, together with the presence of ribosomes on the DMVs' outer membrane (Figure S2C) suggests that DMVs originate from the rough ER. Additionally, smooth ER connectors were seen linking DMVs to the rough ER (Figures 3A–3D, 3H, and 3I; Video S3), corroborating the observations made by the FIB-SEM analysis. With very low frequency, we observed an opening in the DMV membranes (Figure S2D) that connected the DMV interior to the cytosol. Although the presence of such openings could allow for the exchange of metabolites and for the release of newly synthesized viral RNAs into the cytoplasm, their low frequency argues for a very short-lived transition state prior to complete closure of the DMV membrane.

Consistent with recent reports (Klein et al., 2020; Ogando et al., 2020), DMV-DMV contacts were also observed, either through funnel-like junctions between two DMVs (Figure S2E) or by the formation of tabs and indentations in adjacent DMVs that resemble jigsaw puzzle pieces (Figure S2F). Ultimately, these membrane bending events might generate fused DMVs (Figure S2G) consisting of multiple vesicles sharing the same outer membrane, or multimembrane vesicles formed by DMVs that have engulfed either a single- or a double-membrane vesicle (Figure S2H).

Re-organization of the ER network was also confirmed by confocal microscopy of SARS-CoV-2-infected A549 lung epithelial cells overexpressing ACE2. We observed localization of the tubular ER protein Reticulon 3 (RTN3) in the perinuclear region containing high amounts of double-stranded RNA, a marker of viral replication, and the viral protein nsp3 (Figure 3J). Conversely, the Sec61β subunit of the translocon was mostly excluded from this region, indicating that despite the close link of DMVs to the ER, the synthesis of transmembrane or secreted proteins is relocated to the vRO periphery (Figure 3J).

In our datasets, double-membrane spherules, similar to the ones described for other coronaviruses (Snijder et al., 2020), were only rarely seen in SARS-CoV-2-infected cells. These structures had a diameter of ∼75.5 ± 5.9 nm, an electron-dense interior and were linked to the connectors from which they originated (Figures 3K and 3L; Video S4).

Altogether, our 3D reconstruction data provide strong evidence that SARS-CoV-2 reorganizes the ER network and alters the morphology of this organelle to generate vROs, which consist predominantly of DMVs, but also include other ER-derived structures such as ER connectors, double-membrane spherules, and multi-membrane vesicles.

SARS-CoV-2 Infection Reorganizes Peroxisomes, Mitochondria, and the Secretory Apparatus

In addition to the formation of *de novo* ER-derived organelles, SARS-CoV-2 replication alters the morphology, the number, and the function of several other cellular compartments. Of note, in regions containing DMV clusters, we observed accumulation of peroxisomes in close proximity to the DMVs' outer membrane (Figures 4A–4C, S3A, andS3B; Video S5). These re-

sults were confirmed by confocal microscopy and western blot analyses, showing a redistribution of peroxisomes to double-stranded RNA (dsRNA)$^+$ regions (Figures S3C and S3D) and an increase in the peroxisome-associated protein PMP70 in infected cells (Figure S3E). Consistently, super-resolution microscopy revealed an enclosing of the dsRNA signal by the peroxisomal signal (Figure S3F), supporting the topology observed by electron tomography (Figures 4A–4C). The spatial proximity between peroxisomes and the sites of viral RNA replication (Figures S3A and S3B) argues for a role of peroxisomes in the SARS-CoV-2 replication cycle such as the prevention of oxidative damage to viral RNA or an involvement in lipid metabolism (Cook et al., 2019) or serving as signaling platform mounting a cytokine response (Dixit et al., 2010).

Mitochondria were also altered in SARS-CoV-2-infected cells in several ways. First, they were displaced and accumulated at the periphery of dsRNA$^+$ regions (Figure S3G). Second, mitochondria morphology was altered showing an increase of both intracristal space and matrix density, conferring an electron-dense appearance in transmission electron microscopy (Figure S3H). Third, in infected cells, mitochondria were significantly thinner than in uninfected cells (Figure S3I). Forth, in infected cells, we observed a strong decrease in the total amounts of the mitochondrial ATP synthase subunit 5B (ATP5B), a key factor for cellular energy production (Figures S3J and S3K). Altogether, these results reveal strong perturbation of mitochondria morphology and function, most likely reflecting SARS-CoV-2-induced attenuation of cellular energy metabolism.

The high frequency of budding events observed in the Golgi apparatus and the surrounding vesicular membrane compartment indicates that these organelles provide membranes for SARS-CoV-2 assembly (Figures 4D–4F; Video S5). Within these cellular compartments, strings of viral nucleoprotein, corresponding to dark-stained granules were found on bent membranes, which, given the similarities in morphology to fully assembled virions, probably correspond to the early stages of virion budding (Figure S4A). Consistent with previous reports, we also observed fully assembled virions with an average diameter of 80 ± 9.5 nm (Figure S4B) (Klein et al., 2020). The global overview obtained from the large set of tomograms and the FIB-SEM data reveal that assembly sites, corresponding to the Golgi and surrounding vesicles, and DMVs, the RNA replication sites, are in close proximity, suggesting spatiotemporal coordination of the different steps of the SARS-CoV-2 replication cycle (Figures 4A–4F and S1; Videos S1 and S5).

In uninfected cells, the secretory compartment showed well-defined morphology. The polarization of the Golgi stacks allowed for reliable identification of the ER-to-Golgi intermediate compartment (ERGIC) area and the presence of clathrin-coated vesicles marked the *trans*-Golgi network (TGN) site (Figure S4C). Differently, fragmentation and dispersion of the Golgi apparatus, with formation of multiple Golgi ministacks, was observed in SARS-CoV-2-infected cells as early as 6 h after infection (Figures 4G, 4H, S4D, and S4E). Although fragmented Golgi cisternae were found in the vicinity of DMVs (Figures 4D–4F and S1) and might constitute assembly sites, total Golgi area was only marginally reduced (Figure S4E), suggesting that viral infection induced mainly a fragmentation and redistribution of the Golgi cisternae (Figure S1). Due to the altered Golgi morphology,
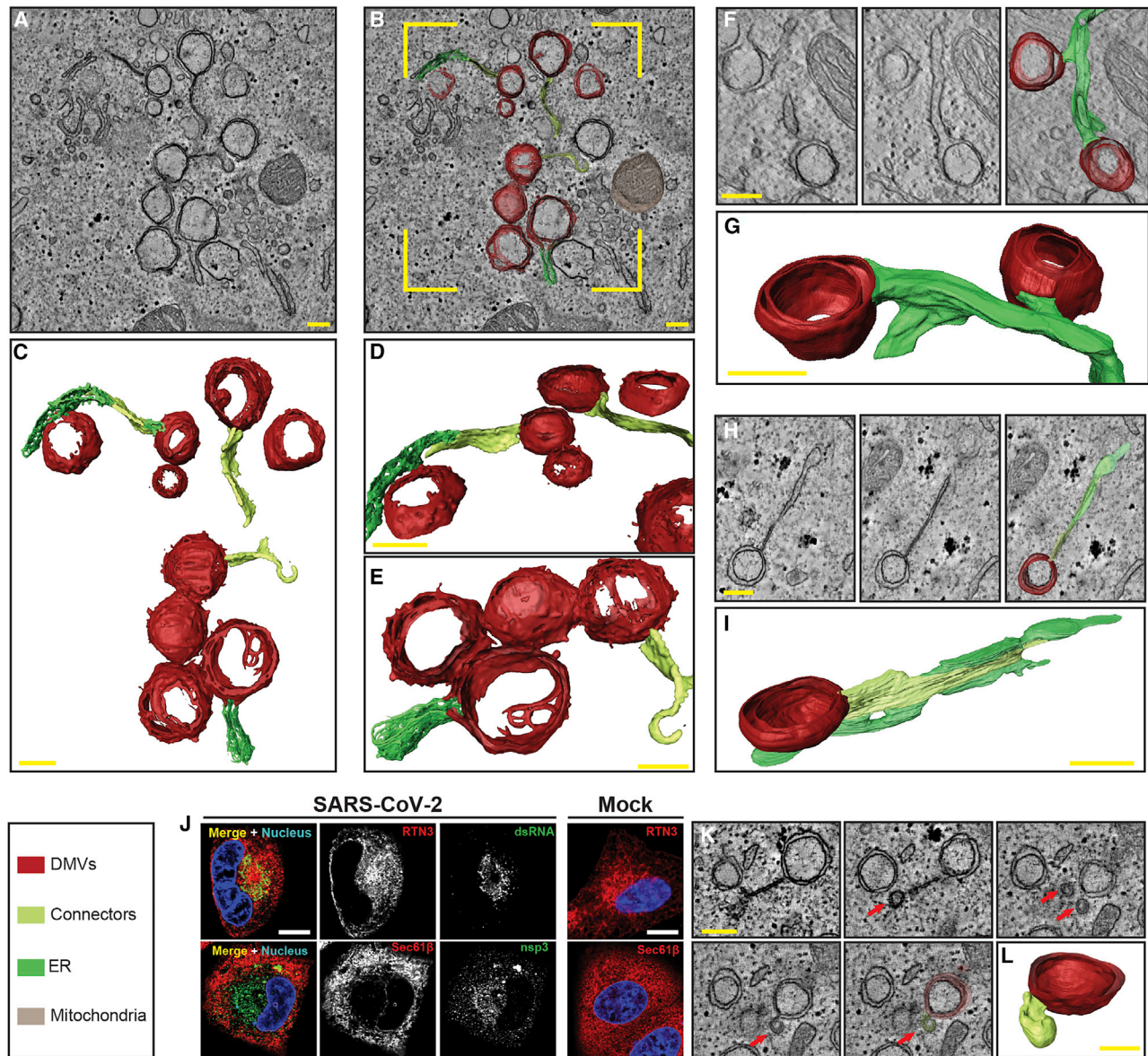
Figure 3. High-Resolution Analysis of ER-DMV Inter-Connectivity and Selective Recruitment of ER-Resident Proteins to Sites of Viral Replication Organelles

Electron tomography and 3D rendering of SARS-CoV-2-infected Calu-3 cells (MOI = 5) harvested 12 h after infection.

(A) Slice through the tomogram.

(B) Same region as in (A) with superimposed rendering of cellular and viral organelles. The color code of visualized structures for this and subsequent panels is given in the lower left of the figure.

(C) 3D reconstruction of the area indicated with yellow rectangle in (B).

(D) Magnified view of DMVs (red) in close contact with membrane connectors (citrus).

(E) Magnified view of a DMV in close contact with the ER (green). An ER connector forming a hook is also visible (bottom right).

(F) Consecutive slices of a tomogram depicting two adjacent DMVs sharing the outer-membrane with the ER.

(G) Side view of the 3D rendering.

(H) Orthogonal slices of a tomogram depicting a membrane connector in contact with a DMV and with the ER. A superposition of rendered DMV and ER is shown on the right.

(I) 3D rendering view of the DMV and its connectivity to the ER. Scale bars, 200 nm.

(J) A549-ACE2 cells were infected with SARS-CoV-2 for 16 h and fixed and stained with primary antibodies of the given specificities. DNA was stained with DAPI (blue). Single slices through deconvoluted z stacks are shown. Scale bar, 10 μm.

(K and L) Consecutive slices (K) and 3D rendering (L) of membrane connector bending to form a double-membrane spherule. Red arrows point to double membrane spherules. Scale bars, 200 nm.

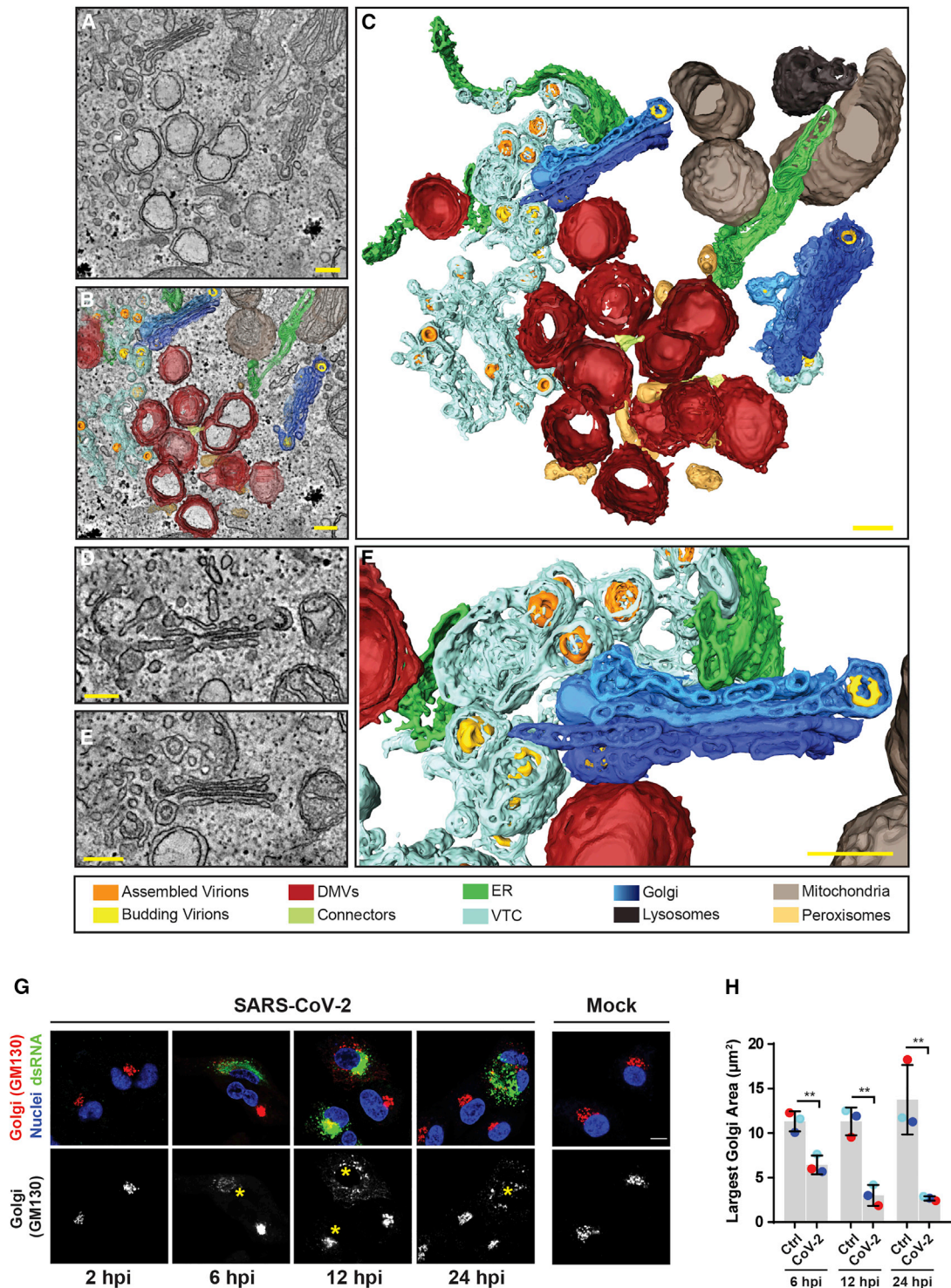See also Figure S2 and Videos S2, S3, and S4.

Figure 4. Spatial Coupling of SARS-CoV-2 Replication and Assembly Sites Mediated by Close Proximity of DMVs, Vesicular-Tubular Compartment and Golgi Apparatus

(A–F) Electron tomography and 3D rendering of SARS-CoV-2-infected Calu-3 cells (MOI = 0.5) harvested 24 h after infection.

(A) Slice through the tomogram.

(B) Same region as in (A) with superimposed rendering of cellular and viral organelles that are specified on the bottom of the figure.

(C) 3D rendering of organelles visualized in (A).

(D–F) Zoom-in view of the vesicular-tubular compartment (VTC) (cyan) and Golgi apparatus (dark blue) with budding virions (yellow), and fully assembled virions (orange). Scale bars, 200 nm.

unambiguous identification of the ERGIC and TGN sites is challenging in SARS-CoV-2-infected cells, and therefore we use the more general term vesicular-tubular compartment (VTC) when referring to the membranes in close proximity of the ER and the Golgi stacks.

In addition to conventional assembly at the VTC and Golgi sites, assembly events were also observed at electron-dense vesicles containing large numbers of virions (Figure S4F, i–iii). Moreover, assembled virions were also present in multivesicular bodies (Figure S4F, iv). Such structures could either provide an alternative secretory route or represent dead-end products of the assembly process.

SARS-CoV-2 Causes Cytoskeleton Remodeling Important for Viral Replication

In addition to the secretory apparatus, mitochondria, and peroxisomes, we also evaluated possible cytoskeleton alterations in SARS-CoV-2-infected cells. To this end, we analyzed different classes of cytoskeletal filaments, i.e., the microtubules, the actin microfilaments, and the intermediate filaments by using A549-ACE2 cells that are superior to Calu-3 cells for light microscopy imaging of these cellular elements. Consistent with a recent report (Bouhaddou et al., 2020), we observed an accumulation of cortical actin at the plasma membrane of the infected cells, suggesting a role for actin in virion release and/or virus spread (Figure 5A). Moreover, large intracellular vesicles containing Spike and surrounded by an actin ring accumulated in SARS-CoV-2-infected cells. In addition, SARS-CoV-2-infected cells exhibited a perinuclear inclusion that stained positive for dsRNA and was surrounded by a cage of intermediate filaments (Figure 5A). This cage was surrounded by microtubules that were excluded from the dsRNA-containing region (Figure 5A), arguing that intermediate filaments might serve to scaffold or confine the vRO compartment. Interestingly, bundles of cytoskeletal filaments were also observed in tomograms of infected Calu-3 cells in close proximity of the vROs (Figures S5A and S5B).

To better resolve the details of the intermediate filaments surrounding the vROs, we performed super-resolution STED microscopy on the whole-cell volume (Figure 5B; Video S6). The dsRNA region was seen mostly devoid of intermediate filaments, except for a few branches that protruded within the vRO region (Figure 5Biii). This arrangement suggests that cytoskeletal elements might be displaced by clusters of DMVs, the main constituents of vROs, or that the cytoskeleton, notably intermediate filaments support vRO formation.

To analyze the dynamics of intermediate filament remodeling in real time, we established a SARS-CoV-2 reporter system (Pahmeier et al., 2020) in which a green fluorescent protein (GFP), tagged with a nuclear localization sequence (NLS), is anchored to the cytosolic side of the ER by the transmembrane domain of Sec61β through a linker containing a recognition sequence for the SARS-CoV-2 main protease 3-chymotrypsin-like (3CL) (Figure 5C, top). Upon infection by SARS-CoV-2, the reporter protein is cleaved by 3CL, releasing the GFP-NLS moiety, which

then translocates into the nucleus. Thus, the nuclear GFP signal serves as an identifier of SARS-CoV-2-infected cells. Co-expression of fluorescently tagged vimentin together with this biosensor allowed for the characterization of intermediate filaments remodeling and cage formation in infected cells by means of live cell imaging (Figure 5C; Video S7). Although spatial information was limited by the resolution of our imaging system, which did not allow visualizing single intermediate filaments, we were able to record the dynamics of cage formation. On average, nuclear translocation of the reporter and vimentin cage formation became detectable at identical time frames, and the majority of events were detected at 6.5 h after infection (Figure 5D). A smaller proportion of GFP translocation events, corresponding to viral spread, were observed at 16 h after infection, suggesting that a complete infection cycle might require ∼9.5–10 h. At this late time point, a peak in cell death, as judged by plasma membrane blebbing and cell disruption, was recorded, which affected only ∼20% of the cells. Therefore, the majority of infected cells were alive at 24 h after infection, indicating that the phenotype we observed was not due to cell death.

To investigate the contribution of the different components of the cytoskeletal network to SARS-CoV-2 replication, we treated infected cells with compounds altering cytoskeleton integrity and dynamics (Figure 6A). For this we used drug concentrations that did not induce cytotoxicity as determined by quantification of intracellular ATP levels (Figure 6B). We observed a robust reduction in viral replication and amount of infectious virus released from cells that were treated for 6 h with Withaferin A, a compound that disrupts the intermediate filaments network (Mohan and Bargagna-Mohan, 2016) (Figures 6C and 6D), arguing for an important role for intermediate filaments in vRO formation. Surprisingly, treatment with latrunculin A, a microfilament-disrupting agent, did not affect viral replication or infectious particle production, suggesting a limited contribution of the actin network to SARS-CoV-2 replication (Figures 6C and 6D). Notably, although nocodazole and colcemid (inducing microtubule depolymerization) did not affect SARS-CoV-2 replication, paclitaxel and vinblastine (inhibiting microtubule depolymerization or polymerization, respectively), had a strong effect on the production of infectious extracellular virus. These results reveal intermediate filaments and microtubules as critical host factors contributing to SARS-CoV-2 replication and virus production, respectively.

DISCUSSION

In this study, we took advantage of several state-of-the-art imaging techniques to determine the 3D architecture and cytoplasmic configuration of SARS-CoV-2 ROs and virus-induced alterations of cellular organelles. Consistent with very recent reports, we confirm that SARS-CoV-2 alters the ER network to generate DMVs similar to other betacoronaviruses such as SARS-CoV-1, MERS-CoV, and MHV (Angelini et al., 2013; Hagemeijer

---

(G) Time course of Golgi fragmentation in SARS-CoV-2-infected (MOI = 5) A549-ACE2 cells. Asterisks indicate infected cells. Scale bar, 10 μm.
(H) Quantification of images in (G). For each cell, the largest Golgi fragment was calculated. Each dot indicates the mean values from at least 30 individual cells. Mean and SD of triplicate experiments are shown. p value was calculated with Student's t test. ** = $p < 0.01$.
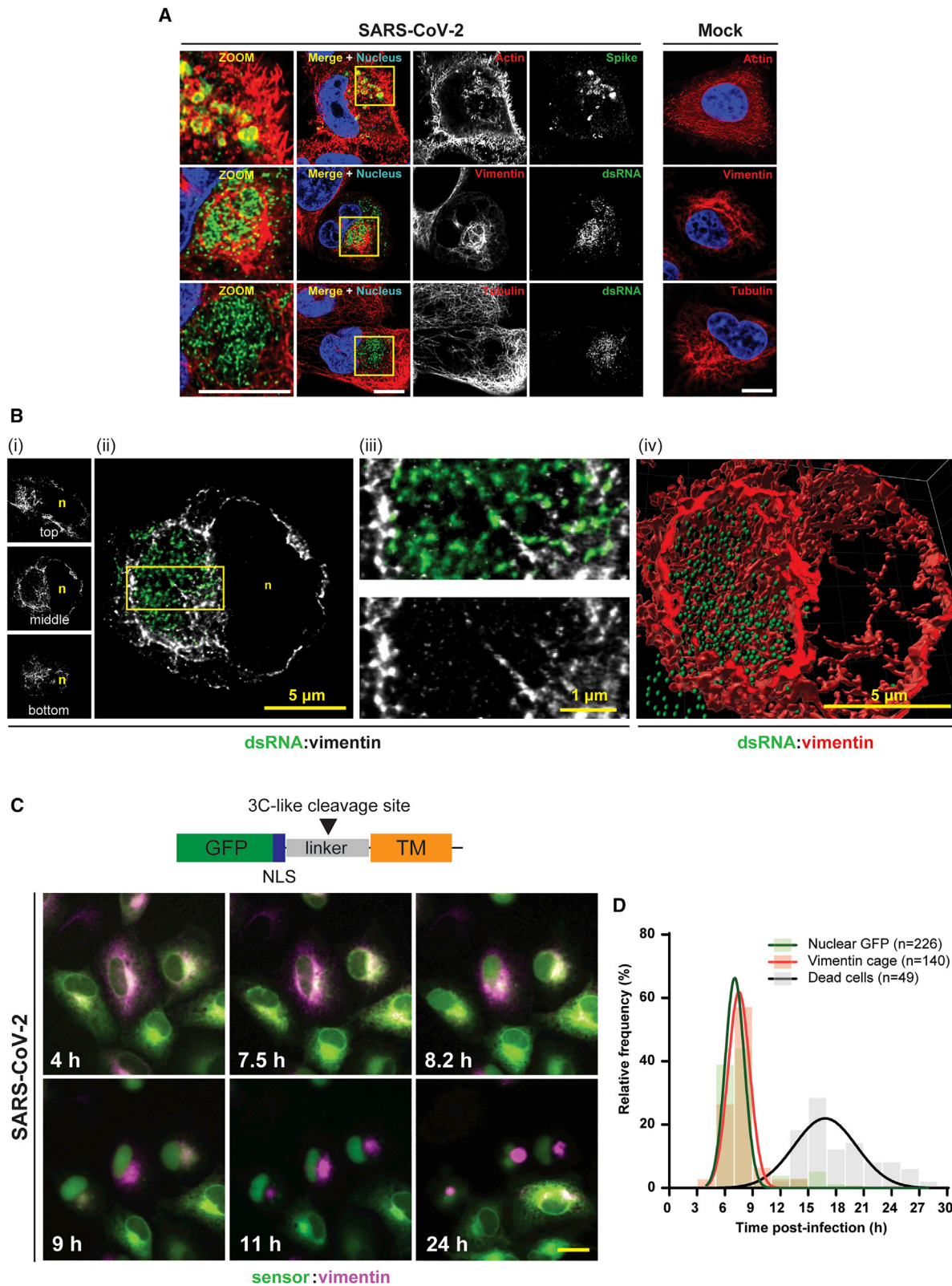See also Figures S1, S2, and S4 and Video S5.

Figure 5. A Network of Intermediate Filaments Surrounds SARS-CoV-2 Replication Organelles

(A) A549-ACE2 cells were infected with SARS-CoV-2 for 16 h (MOI = 5), fixed and stained with antibodies of the given specificities. DNA was stained with DAPI (blue). A single slice through a deconvolved z stack is shown. The regions in the yellow boxes are magnified in the insets on the left. Scale bar, 10 μm.

et al., 2014; Knoops et al., 2008; Snijder et al., 2020; Wolff et al., 2020). Importantly, several 3D volume EM datasets acquired by FIB-SEM and the evaluation by 3D reconstruction of a full volume of an infected cell show that SARS-CoV-2 infection induces a massive spatial reorganization of the cytoplasm to create a network of vROs. DMVs accumulate in the perinuclear region along with fragmented and stacked membranes of the Golgi apparatus as well as peroxisomes. This replication-conducive environment is enclosed by a cage-like structure consisting of intermediate filaments. The DMVs were often interconnected or tethered by ER membranes, largely independent from convoluted membranes that were reported for SARS-CoV-1 and MERS-CoV (Knoops et al., 2008; Snijder et al., 2020). Instead, DMVs were often linked to stretched ER plates with a narrow luminal space. These ER connectors are reminiscent of zippered ER reported for other coronaviruses (Snijder et al., 2020). It is plausible that the lumen of the ER, from which DMVs protrude, collapses, and ER membranes remain connected to DMVs and get stretched as they grow over the course of infection. Alternatively, DMVs might first form at ER ends, followed by collapse of the respective ER tubule.

With a lower frequency than DMVs, we could also detect double-membrane spherules that exhibited a smaller diameter than the one of DMVs (∼75 nm versus ∼300 nm). These structures were often located at the tip of the ER connectors and might result from connector membrane bending and subsequent self-wrapping (Figures 3K and 3L). The absence of viral RNA with double-membrane spherules (Snijder et al., 2020) suggests that these structures do not play a role in viral RNA synthesis but might instead constitute a defective by-product of vRO morphogenesis or exert functions not detectable in *in vitro* cell culture systems.

Several reports have provided convincing evidence that MERS-CoV and SARS-CoV-1 RNA synthesis occurs inside DMVs. Indeed, dsRNA as well as [^{3}H] uridine-labeled *de novo* synthesized RNAs were detected inside DMVs by electron microscopy (Knoops et al., 2008; Snijder et al., 2020). Moreover, very recently, viral RNA has been detected inside DMVs by cryo-electron microscopy (Klein et al., 2020). Consistent with DMVs serving as sites of viral RNA replication, proteinaceous pores have been reconstructed from MHV-induced DMVs, and these pores most likely serve as sites for the exchange of metabolites, such as nucleoside triphosphates, and exit of viral RNA into the cytoplasm (Wolff et al., 2020).

The mechanism underlying DMV biogenesis is poorly understood. Close examination of ∼900 DMVs from more than 200 tomograms identified single openings in just a few of them (Figure S2D; Table S1). Although we cannot exclude that

membrane integrity was compromised during sample preparation, it is tempting to speculate that DMV openings might represent transition states during DMV biogenesis prior to complete membrane closure. Of note, ribosomes were occasionally detected on the cytosolic side of DMVs (Figure S2C), supporting a model in which newly synthesized viral RNAs exiting DMVs are directly used for protein synthesis. Moreover, the spatial organization of DMVs, ER, and the secretory compartment as observed here allows an optimal coordination between RNA synthesis, RNA translation, and virion assembly. Indeed, newly produced nucleocapsid proteins would already be properly localized to associate with genomic RNA as it is exported from DMVs. These viral ribonucleoprotein particles would be subsequently packaged and bud into the nearby VTC neighboring the DMVs. Supporting a tight coordination between viral RNA synthesis and virus assembly, small stacks of fragmented Golgi-like membranes, which contained virions, were often found in the vicinity of DMVs (Figures 4, S1, S4D, and S4E).

Juxtaposed to DMVs, we observed the accumulation of peroxisomes, which were also more abundant in SARS-CoV-2-infected cells than in control cells (Figures S3A–S3F). These organelles might contribute to viral replication, e.g., by reducing oxidative stress that might result from the extensive remodeling of cellular endomembranes by SARS-CoV-2, or by providing additional lipids required for DMV formation (Cook et al., 2019). Finally, the translocon subunit Sec61β, an abundant ER protein, was mostly excluded from the vRO compartment (Figure 3J) strongly suggesting a partitioning of ER functions in infected cells. Consistently, our confocal microscopy analysis of infected cells revealed that the ER-bending protein RTN3 was enriched in the perinuclear region where dsRNA accumulated, arguing that SARS-CoV-2 might hijack distinct ER-shaping proteins for vRO biogenesis. Such host cell factor usurpation has been reported for other RNA viruses. For instance, the ER-shaping proteins atlastin 2, RTN3, and the reticulophagy factor FAM134B were recently shown to be involved in the biogenesis of flavivirus replication organelles (Lennemann and Coyne, 2017; Monel et al., 2019; Neufeldt et al., 2019). It is tempting to speculate that the functions of such host factors might be regulated by nsp3-4 shown for other coronaviruses to be sufficient to induce DMVs (Angelini et al., 2013; Hagemeijer et al., 2014).

Apart from the ER and peroxisomes, several other cellular organelles were found to be remodeled in SARS-CoV-2-infected cells. This includes mitochondria displaying swollen cristae and matrix condensation, along with reduced components of the ATP synthase. This observation is consistent with transcriptional changes reported for SARS-CoV-2-infected cells, indicating reduced oxidative phosphorylation and pointing toward

(B) Cells infected as in (A) were fixed and stained with antibodies directed against dsRNA, the viral replication intermediate, and vimentin. Images were taken by using an Abberior instruments STED microscope. Z stacks comprising whole cells were acquired. Selected slices through the stack are shown in (i). A middle slice with dsRNA (green) and vimentin (gray) signals is shown in (ii). The region in the yellow box is magnified in (iii). A 3D-rendered model of the dsRNA (green) and vimentin (red) signals is shown in (iv).

(C) Live cell imaging of SARS-CoV-2-infected A549-ACE2 cells transiently expressing an mCherry-tagged vimentin protein (magenta) and a GFP-NLS-tagged SARS-CoV-2 fluorescent reporter (the structure of this reporter is given on the top). Infected cells show nuclear translocation of the GFP-NLS reporter. Scale bar, 20 μm. Abbreviations are as follows: NLS, nuclear localization sequence; GFP, green fluorescent protein; TM, transmembrane region of Sec61β. The black arrowhead represents the SARS-CoV-2 3C-like protease cleavage site.

(D) Frequency distribution of the GFP-NLS nuclear translocation (green bars), vimentin peri-nuclear accumulation (red bars) and infected cell death (gray bars) events. Gaussian fit of each dataset is shown.

See also Figure S5 and Videos S6 and S7.
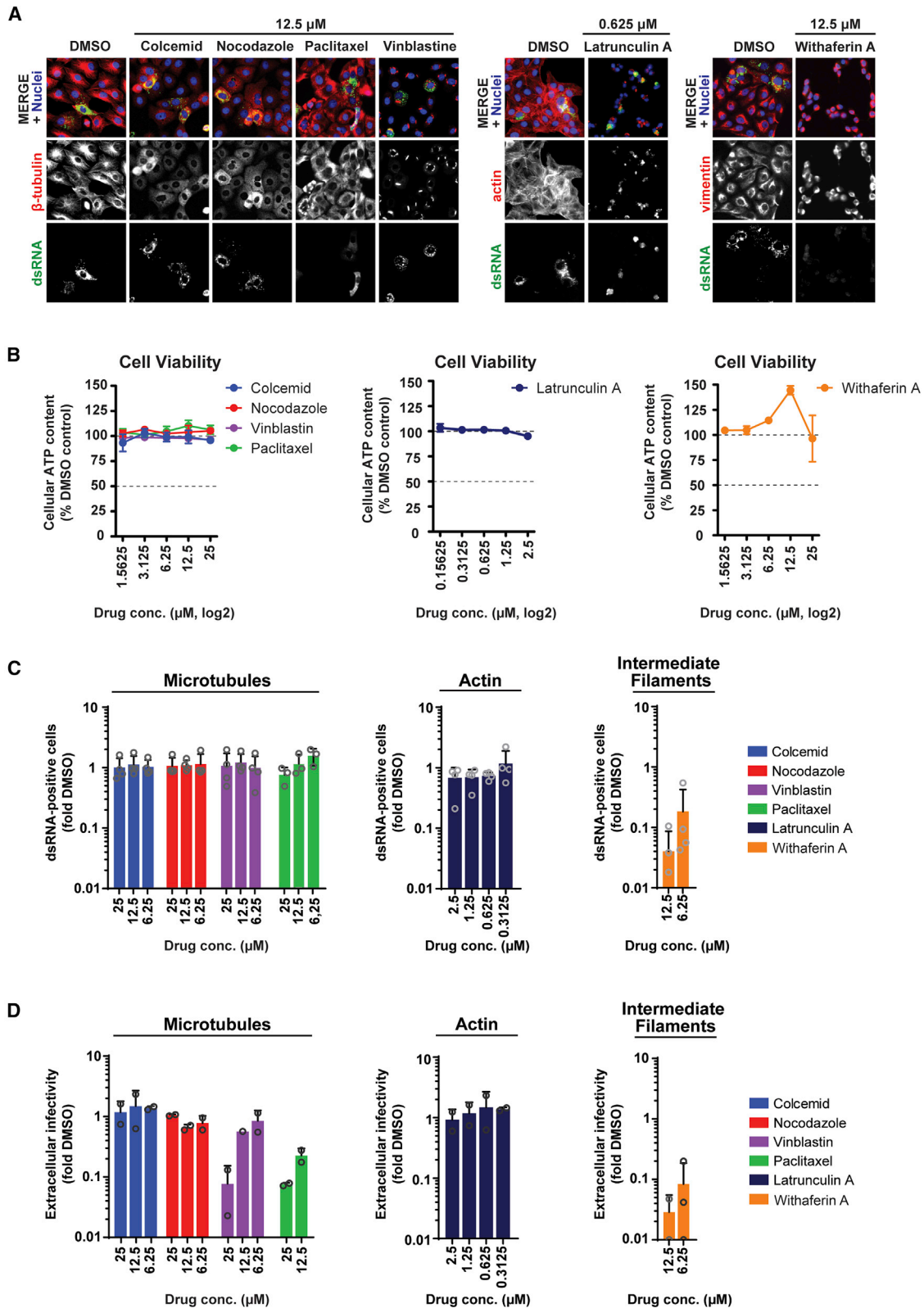
metabolic reprogramming triggered by the virus (Neufeldt et al., 2020).

Nocodazole and colcemid induce microtubule depolymerization and did not affect SARS-CoV-2 replication (Figures 6C and 6D), whereas alteration of microtubule dynamics, either by inhibiting polymerization or depolymerization of the microtubular network, strongly suppressed the production of infectious SARS-CoV-2 (Figure 6D). Paclitaxel induces microtubule bundles that associate with Golgi fragments (Sandoval et al., 1984; Wehland et al., 1983). This might prevent redistribution of Golgi ministacks close to the viral replication sites, the DMVs, thus altering the spatio-temporal coordination of viral replication and assembly. Although other mechanisms might account for the observed phenotype, microtubules play an important role in shaping Golgi structure and function, arguing that the observed reduction in extracellular infectivity is linked to alteration of the assembly or secretion of virus particles at the Golgi. In contrast, disruption of the actin microfilament network with latrunculin A did not affect virus production and spread. Nevertheless, in infected cells we observed a striking redistribution of cortical actin. This might reflect the formation of filopodia suggested to allow rapid spread of SARS-CoV-2 in infected tissues (Bouhaddou et al., 2020).

DMVs concentrate within a cage-like structure, which is induced upon infection and composed of intermediate filaments that might aid in spatial segregation of DMVs in the perinuclear area. It is unknown whether such structures are shared by other coronaviruses, but it is reminiscent of those we have previously reported for Zika virus (Cortese et al., 2017), a positive-strand RNA virus belonging to the *Flaviviridae* family. Live cell imaging and super-resolution microscopy with SARS-CoV-2-infected cells highlighted virus-induced alteration of the vimentin network (Figures 5B and 5C; Videos S6 and S7). Consistently, enforced pharmacological aggregation of intermediate filaments with Withaferin A was detrimental for viral replication supporting that this structure contributes to viral replication (Figure 6C). Of note, a recent systems biology study revealed that the phosphorylation levels of serine residues 39 and 56 of vimentin are decreased in SARS-CoV-2-infected cells (Bouhaddou et al., 2020), and phosphorylation of serine residue 39 has been shown to impede intermediate filament polymerization (Eriksson et al., 2004). In addition, SARS-CoV-2 nsp7 associates with the RhoA kinase of the Rho/Rac/Cdc42 pathway, which positively regulates PAK1/2-dependent phosphorylation of vimentin (Gordon et al., 2020). Altogether, these data provide compelling evidence that SARS-CoV-2 regulates the dynamics of intermediate filaments in infected cells, possibly through the modulation of post-translational modifications. Whether nsp7 is responsible for the observed changes in intermediate filament dynamics and cage formation remains to be determined.

Intermediate filaments also play an important role in innate immunity and induction of a cellular antiviral state (Mostowy and Shenoy, 2015). Interestingly, type I interferon treatment was shown to alter the integrity of arterivirus nsp2/3-induced DMVs (Oudshoorn et al., 2016). This raises the hypothesis that the SARS-CoV-2-induced vimentin cage might reduce access of the viral replication compartment to sensors of the cellular innate defense system. Moreover, the sub-population of vimentin located at the cell surface was shown to contribute to SARS-CoV-1 S-mediated cell entry of virus-like particles (Yu et al., 2016). Although such participation in the entry of genuine virus particles was not investigated, the redistribution of intermediate filaments around the replication compartment and its expected exclusion from the plasma membrane would constitute a mechanism to avoid super-infection or retention of newly synthesized virions at the surface of the virus-producing cells.

In conclusion, this study reports a comprehensive overview of SARS-CoV-2-induced vROs and virus-induced alterations of cellular organelles. We employed an integrative imaging analysis and generated an unprecedented repository of 3D structure information of virus-induced substructures and whole-cell volumes, deduced from a FIB-SEM dataset and around 250 tomograms. All these data will be shared with the scientific community for download through the EMPIAR platform and for smooth online visualization through MoBIE (Vergara et al., 2020). This data-rich resource will support the global investigative effort to study how SARS-CoV-2 interacts with its host and become an important tool to unveil novel antiviral targets for the development of host-targeting drugs suppressing viral replication as well as virus-induced cell damage.

Limitations of the Study

Our study describes morphological changes induced by SARS-CoV-2 in the host cell. Although we used a human-lung-derived cell line that can be used as respiratory model, it remains to be determined how well observed cellular alterations reflect those induced *in vivo*. Moreover, there are several open questions regarding the molecular mechanisms responsible for the observed perturbations. For instance, the biogenesis of SARS-CoV-2 ROs is still poorly characterized, and we do not have detailed information on the host or viral factors that contribute to RO formation. Identification of these factors can provide promising candidates for developing compounds that could limit viral replication. Likewise, further investigation is needed to determine the molecular mechanisms underlying cellular organelle reshaping induced by SARS-CoV-2 infection, such as Golgi fragmentation or cytoskeletal remodeling as well as the association between peroxisomes and viral DMVs. Using our ultrastructural dataset as a foundation, we can begin to design studies aimed at answering these questions that will provide useful

Figure 6. Important Role of the Cytoskeleton for Productive SARS-CoV-2 Replication and Virus Particle Production
(A) Compounds that alter the cytoskeletal network were tested on Vero E6 cells infected with SARS-CoV-2. Infection was allowed to proceed for 2 h prior to addition of given concentrations of the indicated compounds. Cells were fixed at 8 h after infection and dsRNA as well as the indicated cytoskeleton elements were detected by immunofluorescence microscopy using specific antibodies.
(B) Cell viability after 6 h treatment with the indicated compounds as determined by quantification of intracellular ATP levels.
(C) Percentage of infected cells as determined by dsRNA staining of cells treated as in (A).
(D) Amounts of infectious SARS-CoV-2 released into the culture supernatant of cells treated as in (A) was quantified by using plaque assay.
(C) and (D) show means and SDs; each dot represents the mean of technical triplicates (C) or duplicates (D).

insights into SARS-CoV-2 pathogenesis and will allow us to better understand the interplay between the virus and the host cell.

STAR★METHODS

Detailed methods are provided in the online version of this paper and include the following:

- KEY RESOURCES TABLE
- RESOURCE AVAILABILITY
  - Lead Contact
  - Materials Availability
  - Data and Code Availability
- EXPERIMENTAL MODELS AND SUBJECT DETAILS
  - Cell Lines
  - Viruses
- METHOD DETAILS
  - Light Microscopy (Confocal and STED)
  - Live Cell Imaging
  - Plaque Assay
  - Cytotoxicity Measurement
  - Drug Treatments
  - RT-qPCR
  - Sample Processing for TEM
  - Electron Tomography (Sample Acquisition, Reconstruction and Rendering)
  - Sample Preparation for FIB-SEM
  - FIB-SEM
  - Electron Microscopy Dataset Visualization through MoBIE
- STATISTICAL ANALYSIS AND QUANTIFICATION

AUTHOR CONTRIBUTIONS

Project design: M.C., Y.S., and R.B.; EM sample preparation: V.M.J.O., N.L.S., and M.C.; performance of TEM experiments: V.M.J.O. and Y.S.; TEM tomography acquisition: S.K. and M.B.; FIB-SEM acquisition: N.L.S and P.R., with support from K.M., R.M.T., M.S.B., and R.S.M.; design of the FIB-SEM data image analysis: J.H.; image analysis on TEM tomography and FIB-SEM data: S.K., P.R., Y.S., G.M., V.M.J.O., V.G., M.B., K.M., I.R.B., R.S.M., N.L.S., M.S.B., and Y.S.; editing of 3D videos: G.M., J.H., and J.L.; implementation of image visualization tools for TEM tomography and FIB-SEM data: M.S., C.P., and C.T.; live-cell imaging: A.R.; image analysis light microscopy: J.L., J.F., and M.C.; investigation: M.C., B.C., C.J.N., and N.H.; STED acquisition and analysis: V.L.; manuscript writing: M.C., C.J.N., R.B., and L.C.C.; resources: Y.S., S.B., and M.S.; Data visualization: M.C., A.R., and J.H.; Project supervision: Y.S. and R.B.; Funding: Y.S. and R.B.

DECLARATION OF INTERESTS

The authors declare no competing interests.

REFERENCES

Angelini, M.M., Akhlaghpour, M., Neuman, B.W., and Buchmeier, M.J. (2013). Severe acute respiratory syndrome coronavirus nonstructural proteins 3, 4, and 6 induce double-membrane vesicles. MBio *4*, e00524-13.

Beier, T., Pape, C., Rahaman, N., Prange, T., Berg, S., Bock, D.D., Cardona, A., Knott, G.W., Plaza, S.M., Scheffer, L.K., et al. (2017). Multicut brings automated neurite segmentation closer to human performance. Nat. Methods *14*, 101–102.

Belevich, I., Joensuu, M., Kumar, D., Vihinen, H., and Jokitalo, E. (2016). Microscopy Image Browser: A Platform for Segmentation and Analysis of Multidimensional Datasets. PLoS Biol. *14*, e1002340.

Bouhaddou, M., Memon, D., Meyer, B., White, K.M., Rezelj, V.V., Correa Marrero, M., Polacco, B.J., Melnyk, J.E., Ulferts, S., Kaake, R.M., et al. (2020). The Global Phosphorylation Landscape of SARS-CoV-2 Infection. Cell *182*, 685–712.

Chu, H., Chan, J.F.-W., Yuen, T.T.-T., Shuai, H., Yuan, S., Wang, Y., Hu, B., Yip, C.C.-Y., Tsang, J.O.-L., Huang, X., et al. (2020). Comparative tropism, replication kinetics, and cell damage profiling of SARS-CoV-2 and SARS-CoV with implications for clinical manifestations, transmissibility, and laboratory studies of COVID-19: an observational study. Lancet Microbe *1*, e14–e23.

Çiçek, Ö., Abdulkadir, A., Lienkamp, S.S., Brox, T., and Ronneberger, O. (2016). 3D U-Net: Learning Dense Volumetric Segmentation from Sparse Annotation. Paper presented at: Medical Image Computing and Computer-Assisted Intervention – MICCAI 2016 (Cham: Springer International Publishing).

Cook, K.C., Moreno, J.A., Jean Beltran, P.M., and Cristea, I.M. (2019). Peroxisome Plasticity at the Virus-Host Interface. Trends Microbiol. *27*, 906–914.

Cortese, M., Goellner, S., Acosta, E.G., Neufeldt, C.J., Oleksiuk, O., Lampe, M., Haselmann, U., Funaya, C., Schieber, N., Ronchi, P., et al. (2017). Ultrastructural Characterization of Zika Virus Replication Factories. Cell Rep. *18*, 2113–2123.

Dixit, E., Boulant, S., Zhang, Y., Lee, A.S., Odendall, C., Shum, B., Hacohen, N., Chen, Z.J., Whelan, S.P., Fransen, M., et al. (2010). Peroxisomes are signaling platforms for antiviral innate immunity. Cell *141*, 668–681.

Eriksson, J.E., He, T., Trejo-Skalli, A.V., Härmälä-Braskén, A.S., Hellman, J., Chou, Y.H., and Goldman, R.D. (2004). Specific in vivo phosphorylation sites determine the assembly dynamics of vimentin intermediate filaments. J. Cell Sci. *117*, 919–932.

Gordon, D.E., Jang, G.M., Bouhaddou, M., Xu, J., Obernier, K., White, K.M., O'Meara, M.J., Rezelj, V.V., Guo, J.Z., Swaney, D.L., et al. (2020). A SARS-CoV-2 protein interaction map reveals targets for drug repurposing. Nature *583*, 459–468.

Hagemeijer, M.C., Monastyrska, I., Griffith, J., van der Sluijs, P., Voortman, J., van Bergen en Henegouwen, P.M., Vonk, A.M., Rottier, P.J., Reggiori, F., and de Haan, C.A. (2014). Membrane rearrangements mediated by coronavirus nonstructural proteins 3 and 4. Virology *458-459*, 125–135.

Hennies, J., Lleti, J.M.S., Schieber, N.L., Templin, R.M., Steyer, A.M., and Schwab, Y. (2020). AMST: Alignment to Median Smoothed Template for Focused Ion Beam Scanning Electron Microscopy Image Stacks. Sci. Rep. *10*, 2004.

Hoffmann, M., Kleine-Weber, H., Schroeder, S., Kruger, N., Herrler, T., Erichsen, S., Schiergens, T.S., Herrler, G., Wu, N.H., Nitsche, A., et al. (2020). SARS-CoV-2 Cell Entry Depends on ACE2 and TMPRSS2 and Is Blocked by a Clinically Proven Protease Inhibitor. Cell *181*, 271–280.

Huang, C., Wang, Y., Li, X., Ren, L., Zhao, J., Hu, Y., Zhang, L., Fan, G., Xu, J., Gu, X., et al. (2020). Clinical features of patients infected with 2019 novel coronavirus in Wuhan, China. Lancet *395*, 497–506.

Klein, S., Cortese, M., Winter, S.L., Wachsmuth-Melm, M., Neufeldt, C.J., Cerikan, B., Stanifer, M.L., Boulant, S., Bartenschlager, R., and Chlanda, P. (2020). SARS-CoV-2 structure and replication characterized by *in situ* cryo-electron tomography. bioRxiv. https://doi.org/10.1101/2020.06.23.167064.

Knoops, K., Kikkert, M., Worm, S.H., Zevenhoven-Dobbe, J.C., van der Meer, Y., Koster, A.J., Mommaas, A.M., and Snijder, E.J. (2008). SARS-coronavirus replication is supported by a reticulovesicular network of modified endoplasmic reticulum. PLoS Biol. *6*, e226.

Kremer, J.R., Mastronarde, D.N., and McIntosh, J.R. (1996). Computer visualization of three-dimensional image data using IMOD. J. Struct. Biol. *116*, 71–76.

Lennemann, N.J., and Coyne, C.B. (2017). Dengue and Zika viruses subvert reticulophagy by NS2B3-mediated cleavage of FAM134B. Autophagy *13*, 322–332.

Limaye, A. (2012). Drishti: a volume exploration and presentation tool, *Vol. 8506* (SPIE).

Lowe, D.G. (2004). Distinctive Image Features from Scale-Invariant Keypoints. Int. J. Comput. Vis. *60*, 91–110.

Marzolini, C., Stader, F., Stoeckle, M., Franzeck, F., Egli, A., Bassetti, S., Hollinger, A., Osthoff, M., Weisser, M., Gebhard, C.E., et al. (2020). Effect of Systemic Inflammatory Response to SARS-CoV-2 on Lopinavir and Hydroxychloroquine Plasma Concentrations. Antimicrob. Agents Chemother. *64*, e01177-20.

Mastronarde, D.N. (2005). Automated electron microscope tomography using robust prediction of specimen movements. J. Struct. Biol. *152*, 36–51.

Mastronarde, D.N., and Held, S.R. (2017). Automated tilt series alignment and tomographic reconstruction in IMOD. J. Struct. Biol. *197*, 102–113.

Mohan, R., and Bargagna-Mohan, P. (2016). Chapter Eight - The Use of Withaferin A to Study Intermediate Filaments. In Methods in Enzymology, M.B. Omary and R.K.H. Liem, eds. (Academic Press), pp. 187–218.

Monel, B., Rajah, M.M., Hafirassou, M.L., Sid Ahmed, S., Burlaud-Gaillard, J., Zhu, P.P., Nevers, Q., Buchrieser, J., Porrot, F., Meunier, C., et al. (2019). Atlastin Endoplasmic Reticulum-Shaping Proteins Facilitate Zika Virus Replication. J. Virol. *93*, e01047-19.

Mostowy, S., and Shenoy, A.R. (2015). The cytoskeleton in cell-autonomous immunity: structural determinants of host defence. Nat. Rev. Immunol. *15*, 559–573.

Neufeldt, C.J., Cortese, M., Scaturro, P., Cerikan, B., Wideman, J.G., Tabata, K., Moraes, T., Oleksiuk, O., Pichlmair, A., and Bartenschlager, R. (2019). ER-shaping atlastin proteins act as central hubs to promote flavivirus replication and virion assembly. Nat. Microbiol. *4*, 2416–2429.

Neufeldt, C.J., Cerikan, B., Cortese, M., Frankish, J., Lee, J.-Y., Plociennikowska, A., Heigwer, F., Joecks, S., Burkart, S.S., Zander, D.Y., et al. (2020). SARS-CoV-2 infection induces a pro-inflammatory cytokine response through cGAS-STING and NF-kB. bioRxiv. https://doi.org/10.1101/2020.07.21.212639.

Ogando, N.S., Dalebout, T.J., Zevenhoven-Dobbe, J.C., Limpens, R.W.A.L., van der Meer, Y., Caly, L., Druce, J., de Vries, J.J.C., Kikkert, M., Bárcena, M., et al. (2020). SARS-coronavirus-2 replication in Vero E6 cells: replication kinetics, rapid adaptation and cytopathology. J. Gen. Virol. *101*, 925–940.

Otsu, N. (1979). A Threshold Selection Method from Gray-Level Histograms. IEEE Trans. Syst. Man Cybern. *9*, 62–66.

Oudshoorn, D., van der Hoeven, B., Limpens, R.W., Beugeling, C., Snijder, E.J., Bárcena, M., and Kikkert, M. (2016). Antiviral Innate Immune Response Interferes with the Formation of Replication-Associated Membrane Structures Induced by a Positive-Strand RNA Virus. MBio *7*, e01991-16.

Pahmeier, F., Neufeldt, C.J., Cerikan, B., Prasad, V., Pape, C., Laketa, V., Ruggieri, A., Bartenschlager, R., and Cortese, M. (2020). A versatile reporter system to monitor virus infected cells and its application to dengue virus and SARS-CoV-2. bioRxiv. https://doi.org/10.1101/2020.08.31.276683.

Pape, C., Remme, R., Wolny, A., Olberg, S., Wolf, S., Cerrone, L., Cortese, M., Klaus, S., Lucic, B., Ullrich, S., et al. (2020). Microscopy-based assay for semi-quantitative detection of SARS-CoV-2 specific antibodies in human sera. bioRxiv. https://doi.org/10.1101/2020.06.15.152587.

Paul, D., and Bartenschlager, R. (2013). Architecture and biogenesis of plus-strand RNA virus replication factories. World J. Virol. *2*, 32–48.

Perlman, S., and Masters, P.S. (2020). Coronaviridae: The viruses and their replication, *Vol. 1*, 7th Edition.

Sandoval, I.V., Bonifacino, J.S., Klausner, R.D., Henkart, M., and Wehland, J. (1984). Role of microtubules in the organization and localization of the Golgi apparatus. J. Cell Biol. *99*, 113s–118s.

Schindelin, J., Arganda-Carreras, I., Frise, E., Kaynig, V., Longair, M., Pietzsch, T., Preibisch, S., Rueden, C., Saalfeld, S., Schmid, B., et al. (2012). Fiji: an open-source platform for biological-image analysis. Nat. Methods *9*, 676–682.

Schneider, C.A., Rasband, W.S., and Eliceiri, K.W. (2012). NIH Image to ImageJ: 25 years of image analysis. Nat. Methods *9*, 671–675.

Schorb, M., Haberbosch, I., Hagen, W.J.H., Schwab, Y., and Mastronarde, D.N. (2019). Software tools for automated transmission electron microscopy. Nat. Methods *16*, 471–477.

Snijder, E.J., Limpens, R.W.A.L., de Wilde, A.H., de Jong, A.W.M., Zevenhoven-Dobbe, J.C., Maier, H.J., Faas, F.F.G.A., Koster, A.J., and Bárcena, M. (2020). A unifying structural and functional model of the coronavirus replication organelle: Tracking down RNA synthesis. PLoS Biol. *18*, e3000715.

Tang, D., Comish, P., and Kang, R. (2020). The hallmarks of COVID-19 disease. PLoS Pathog. *16*, e1008536.

Vergara, H.M., Pape, C., Meechan, K.I., Zinchenko, V., Genoud, C., Wanner, A.A., Titze, B., Templin, R.M., Bertucci, P.Y., Simakov, O., et al. (2020). Whole-body integration of gene expression and single-cell morphology. bioRxiv. https://doi.org/10.1101/2020.02.26.961037.

Wehland, J., Henkart, M., Klausner, R., and Sandoval, I.V. (1983). Role of microtubules in the distribution of the Golgi apparatus: effect of taxol and micro-injected anti-alpha-tubulin antibodies. Proc. Natl. Acad. Sci. USA *80*, 4286–4290.

Wolff, G., Limpens, R.W.A.L., Zevenhoven-Dobbe, J.C., Laugks, U., Zheng, S., de Jong, A.W.M., Koning, R.I., Agard, D.A., Grünewald, K., Koster, A.J., et al. (2020). A molecular pore spans the double membrane of the coronavirus replication organelle. bioRxiv. https://doi.org/10.1101/2020.06.25.171686.

Wrapp, D., Wang, N., Corbett, K.S., Goldsmith, J.A., Hsieh, C.-L., Abiona, O., Graham, B.S., and McLellan, J.S. (2020). Cryo-EM structure of the 2019-nCoV spike in the prefusion conformation. Science *367*, 1260–1263.

Yu, Y.T., Chien, S.C., Chen, I.Y., Lai, C.T., Tsay, Y.G., Chang, S.C., and Chang, M.F. (2016). Surface vimentin is critical for the cell entry of SARS-CoV. J. Biomed. Sci. *23*, 14.

Hanslovsky, P., Pisarev, I., Leite, V., Saalfeld, S., Funke, J., tpietzsch, Günther, U., Bogovic, J., Constantin, P., Schmidt, U.; The Gitter Badger, and Nunez-Iglesias, J. (2020). saalfeldlab/paintera paintera-0.24.0 (Version paintera-0.24.0) (Zenodo). https://doi.org/10.5281/zenodo.372486.

STAR★METHODS

KEY RESOURCES TABLE

REAGENT or RESOURCE	SOURCE	IDENTIFIER
Antibodies		
J2 mouse anti-dsRNA	Scicons	Cat#10010500; RRID: AB_2651015
anti-SARS-CoV-2 Nucleocapsid	Sino Biological	Cat#40143-MM05; RRID: AB_2827977
anti-SARS-CoV spike	Genetex	Cat#GTX632604-100; RRID: AB_2864418
anti-PMP70	Abcam,	Cat#ab3421; RRID: AB_2219901
anti-GM130	Cell Signaling	Cat#12480; RRID: AB_2797933
anti-TGN46	Biorad,	Cat#AHP500G; RIID: AB_323104
anti-tubulin	ThermoFischer	Cat#MA5-17193; RIID: AB_2538664
rabbit anti-vimentin	Abcam	Cat#ab188499; RIID: AB_2747778
anti-RTN3	Santa Cruz	Cat#sc-374599; RIID: AB_10986405
STAR RED, goat anti-mouse IgG, 500 μl	Abberior	Cat#STRED-1001
STAR RED, goat anti-rabbit IgG, 500 μl	Abberior	Cat#STRED-1002
Anti-Mouse IgG - Atto 594 antibody produced in goat	Sigma Aldrich	Cat#76085; RRID: AB_1137653
Anti-Rabbit IgG - Atto 594 antibody produced in goat	Sigma Aldrich	Cat#77671; RRID: AB_1137663
Alexa Fluor 488 donkey anti-mouse IgG	ThermoFischer	A-21202; RRID: AB_141607
Alexa Fluor 488 donkey anti-mouse IgG2a	ThermoFischer	A-21131; RRID: AB_2535771
Alexa Fluor 568 donkey anti-rabbit IgG	ThermoFischer	A-10042; RRID: AB_2534017
Alexa Fluor 568 donkey anti-mouse IgG1	ThermoFischer	A-21124; RRID: AB_2535766
Alexa Fluor 647 donkey anti-rabbit IgG	ThermoFischer	A_31573; RRID: AB_2536183
Bacterial and Virus Strains		
SARS-CoV-2 (isolate Bavpat1/2020)	European Virology Archive	Ref-SKU: 026V-03883
Chemicals, Peptides, and Recombinant Proteins		
565-ATTO conjugated phalloidin	Sigma Aldrich	Cat#94072
Paclitaxel	Sigma Aldrich	Cat#T7402
Nocodazole	Sigma Aldrich	Cat#M1404
Colcemid	Enzo life sciences	Cat#ALX-430-033
Vinblastine	Sigma Aldrich	Cat#V1377
Latrunculin A	Santa Cruz	Cat# sc-202691
Withaferin A	Abcam	Cat#ab120644
Critical Commercial Assays		
CellTiter-Glow	Promega	Cat#G9241
Deposited Data		
Raw and analyzed data	This paper	EMPIAR: 10490
Additional Supplemental Items	This paper	Mendeley Data: https://doi.org/10.17632/8fc7fr8g63.1
Experimental Models: Cell Lines		
Vero clone E6	ATCC	Cat.#CRL-1586
A549	ATCC	Cat.#CCL-185
HEK293T	ATCC	Cat.#CRL-3216
Calu-3	ATCC	Cat.#HTB-55
A549-ACE2	Klein et al., 2020	N/A

(Continued on next page)

Continued

REAGENT or RESOURCE	SOURCE	IDENTIFIER
Oligonucleotides		
RT-qPCR SARS-CoV-2 N Forward: GCCTCTTCTCGTTCCTCATCAC	This paper	N/A
RT-qPCR SARS-CoV-2 N Reverse: AGCAGCATCACCGCCATTG	This paper	N/A
RT-qPCR HPRT Forward: CCTGGCGTCGTGATTAGTG	This paper	N/A
RT-qPCR HPRT Reverse: ACACCCTTTCCAAATCCTCAG	This paper	N/A
Recombinant DNA		
pCMV-Gag-Pol	Gift from Didier Trono	N/A
pMD2-VSV-G	Gift from Didier Trono	N/A
pWPI-mCherryVimentin	This study	N/A
pWPI-RC_CoV-2	Pahmeier et al., 2020	N/A
Software and Algorithms		
ImageJ – Fiji 1.52 s	Schneider et al., 2012	https://imagej.nih.gov/ij/
GraphPad Prism 7.04	GraphPad	https://www.graphpad.com/scientific-software/prism/
Imaris 9.3.0	Oxford Instruments	https://imaris.oxinst.com/
AMIRA 2020.1	Thermo Scientific	https://thermofisher.com/amira-avizo
IMOD – 4.10.42	Kremer et al., 1996; Mastronarde and Held, 2017	https://bio3d.colorado.edu/imod/
Microscopy Image Browser 2.61	Belevitch et al., 2016	http://mib.helsinki.fi/downloads.html
Drishti 2.6.3	Limaye, 2012	https://github.com/nci/drishti/
Paintera 0.24.0	N/A	https://github.com/saalfeldlab/paintera
MoBIE	Vergara et al., 2020	https://github.com/mobie/mobie-viewer-fiji
SerialEM	Mastronarde, 2005; Schorb et al., 2019	https://bio3d.colorado.edu/SerialEM/

RESOURCE AVAILABILITY

Lead Contact

Further information and requests for resources and reagents should be directed to and will be fulfilled by the lead contact, Ralf Bartenschlager (ralf.bartenschlager@med.uni-heidelberg.de).

Materials Availability

Plasmids and/or cell lines will be distributed under the terms of a material transfer agreement.

Data and Code Availability

The tomograms and FIB-SEM datasets generated during this study are available at EMPIAR (ID 10490). Links to the individual tomograms are available in Table S1. Additional Supplemental Items are available from Mendeley Data: https://doi.org/10.17632/8fc7fr8g63.1.

EXPERIMENTAL MODELS AND SUBJECT DETAILS

Cell Lines

VeroE6, A549 and HEK293T cells were obtained from ATCC and grown in complete Dulbecco's modified Eagle medium (DMEM) containing 10% fetal calf serum (FCS), 2 mM L-glutamine, non-essential amino acids, 100 U/mL penicillin and 100 μg/mL streptomycin. Calu-3 cells (a kind gift from Dr. Manfred Frey, Mannheim) were grown in complete DMEM with a final concentration of 20% FCS and supplemented with 10 mM sodium pyruvate. A549 cells stably expressing ACE2 (A549-ACE2) were generated as described recently (Klein et al., 2020).

Viruses

The SARS-CoV-2 isolate Bavpat1/2020 was kindly provided by Prof. Christian Drosten (Charité Berlin, Germany) through the European Virology Archive (Ref-SKU: 026V-03883) at passage 2. Working virus stocks were generated by passaging the virus two times in VeroE6 cells.

METHOD DETAILS

Light Microscopy (Confocal and STED)

For light microscopy Calu-3 cells or A549-ACE2 cells were seeded onto glass coverslips one day prior to infection with SARS-CoV-2. Samples were fixed with 4% paraformaldehyde buffered in PBS for 30 min at room temperature (RT). Plates containing the coverslips were submerged in 6% formaldehyde for 30 min at RT before being transported outside the biosafety level 3 (BSL3) area. Samples were then washed in PBS, permeabilized with 0.1% Triton X-100 in PBS for 10 min at RT, blocked with 5% milk in PBST (PBS with 0.01% Tween-20) for 1 h and incubated with primary antibodies for an additional 60 min at RT in 5% milk-PBST blocking buffer. Samples were washed 3 times in PBST and incubated with Alexa Fluor conjugated secondary antibodies for 45 min at RT in PBST. Samples were washed 3 times in PBST, twice in PBS and mounted with Fluoromount-G mounting medium containing DAPI (Southern Biotechnology). Imaging was performed using a 63x oil immersion objective (NA, 1.4; Leica APO CS2) on a Leica SP8 system with lighting configuration.

Primary antibodies used in this study were: J2 mouse anti-dsRNA (Scicons, # 10010500); mouse anti-SARS-CoV-2 Nucleocapsid (Sino Biological, # 40143-MM05); mouse anti-SARS-CoV spike (Genetex, GTX632604-100), mouse anti-RTN3 (Santa-Cruz, #sc-374599), rabbit anti-PMP70 (abcam, ab3421), rabbit anti-GM130 (cell signaling, #12480), sheep anti-TGN46 (biorad, AHP500G), mouse anti-tubulin (ThermoFischer, # MA5-17193), rabbit anti-vimentin (abcam, #ab188499). For actin staining, 565-ATTO conjugated phalloidin was diluted in 500 μl of methanol according to the manufacturer's instructions (Sigma, #94072) and added together with the secondary antibodies. Alexa Fluor 488, 568 and 647 fluorescent-dye conjugated secondary antibodies were used in this study.

For stimulated emission depletion (STED) microscopy, samples were prepared as described above except that high-precision coverslips were used (Paul Marienfeld GmbH, # 0117520) and secondary antibodies were conjugated either with STAR-RED, ATTO-590 or ATTO-594. Dual-color 2D stimulated emission depletion (STED) microscopy was performed on an Expert Line STED system (Abberior Instruments GmbH, Göttingen, Germany), using a 100x oil immersion objective (NA, 1.4; Olympus UPlanSApo) and excitation with the 590- and 640-nm laser lines. 775 nm STED laser (15% of the maximal power of 3 mW) was used for depletion with pixel dwell time of 10 to 15 μs and 15-nm xy sampling. For 3D STED data, 40% of the STED laser power was used for fluorescence depletion in the Z axis and DyMIN illumination scheme was used to minimize bleaching. Sampling frequency was 30 nm in xy and 70 nm in z axis (xyz). STED images were restored with Huygens Deconvolution (Scientific Volume Imaging) using Classic Maximum Likelihood Estimation (CMLE) algorithm and Deconvolution Express mode with Conservative settings. The 3D rendering and the video of the vimentin staining were generated in IMARIS v8.0 (Oxford instruments).

Live Cell Imaging

The SARS-CoV-2 reporter construct used for live cell imaging will be described in detail elsewhere (Pahmeier et al., 2020). In brief, it is an engineered fusion protein composed of (from N- to C terminus) green fluorescence protein, the nuclear localization sequence from simian virus 40, a linker sequence containing the consensus cleavage site of the 3CL protease of SARS-CoV-1, and the transmembrane region of Sec61β. Lentiviruses encoding the SARS-CoV-2 reporter and mCherry-tagged vimentin were generated by transfecting HEK293T cells with pWPI-RC_CoV-2 and pWPI-mCherryVimentin, respectively, and with helper plasmids pMD2-VSV-G and pCMV-Gag-Pol (gift from Didier Trono). After 48 h post-transfection, supernatants containing lentiviruses were harvested and filtered through a 0.45 μm filter and stored at −80°C. For live cell imaging, A549-ACE2 cells were transduced with lentiviruses encoding for the SARS-CoV-2 reporter and a mCherry-tagged vimentin and seeded onto 35 mm diameter dishes with polymer coated bottom and sealable lid (ibidi, # 81156). 16 h post-transduction, cells were infected with SARS-CoV-2 (MOI = 5) in growth medium without phenol-red. The lid was locked and sealed with silicon to prevent evaporation. 3 h after infection, imaging of cells was started using a Nikon Eclipse Ti inverted microscope, equipped with a 20x objective. Multiple fields were defined and image acquisition was performed at intervals of 10 min for 24 h by using the automated Nikon perfect focus system. Images were analyzed with the Nikon NIS Element Advanced Research program.

Plaque Assay

Plaque assay was performed as previously described (Klein et al., 2020). Briefly, VeroE6 cells seeded in duplicate wells were inoculated with serial 10-fold dilutions of SARS-CoV-2 containing supernatants for 1 h at 37°C. One h later, the inoculum was replaced by serum-free MEM (GIBCO, Life Technologies) containing 0.8% carboxymethylcellulose (Sigma-Aldrich). Samples were fixed three days after infection with formaldehyde, directly added to the medium to a final concentration of 5% for 30 min. Plates were plunged in 6% formaldehyde for inactivation and transported outside the BSL3 area. Plates were then washed extensively with water before being stained with 1% crystal violet and 10% ethanol for 30 min. Plates were rinsed with water, the number of plaques was counted and virus titers were calculated.

Cytotoxicity Measurement

VeroE6 cells were seeded into 96-well plates at a confluency of 7E+03 cells per well and treated for 6 h with serial 2-fold dilutions of the different compounds. For latrunculinA, the highest used concentration was 5 μM, for all the other compounds a starting concentration of 50 μM was used. Nocodazole, paclitaxel and vinblastine were purchased from Sigma. LatrunculinA was obtained from Santa Cruz Biotechnology. WithaferinA was obtained from Abcam. DMSO was used as control. Cell viability was determined by quantitation of ATP concentration using the CellTiter-Glo assay (Promega) as recommended by the manufacturer. A Mithras LB 940 plate reader (Berthold Industries) was used to measure the luminescence. A compound concentration that reduced the ATP amounts more than 20% was considered cytotoxic.

Drug Treatments

VeroE6 cells were seeded in triplicates at a confluency of 7E+03 cells per well in black-wall glass-bottom 96 well plates (Corning, # 353219). Cells were infected with SARS-CoV-2 (MOI = 5) for 1 h at 37°C. At 2 h after infection, virus inoculum was removed, cells were washed with PBS and media containing different concentrations of the compounds were added to the cells. DMSO was used as control. 8 h after infection, virus supernatants were harvested and used for plaque assay. Infected cells were washed in PBS, fixed in 6% formaldehyde, processed for immunofluorescence as described above and imaged as previously reported (Pape et al., 2020).

RT-qPCR

Total RNA was isolated with the Nucleospin RNA extraction kit (Macherey-Nagel) according to the manufacturer's instructions. A high capacity cDNA reverse transcription kit (ThermoFisher) was used for cDNA synthesis from that total RNA. cDNA samples were diluted 1:15 and used for qPCR with the iTaq Universal SYBR green mastermix (Biorad). Primers used in this study were: SARS-CoV-2-N (forward) 5′-GCCTCTTCTCGTTCCTCATCAC-3′, SARS-CoV-2-N (reverse) 5′-AGCAGCATCACCGCCATTG-3′, HPRT (forward) 5′-CCTGGCGTCGTGATTAGTG-3′ and HPRT (reverse) 5′-ACACCCTTTCCAAATCCTCAG-3′. Relative abundance of each specific RNA was determined by correcting the cycle threshold values for the PCR efficiency of each primer set and normalizing to the hypoxanthine phosphoribosyltransferase 1 (HPRT) transcript levels.

Sample Processing for TEM

Calu-3 cells grown on glass coverslips were infected with SARS-CoV-2 either at MOI = 5 or MOI = 0.5 as specified in the results section. Cells were fixed by adding 2x concentrated EM fixative (composition of the 1x fixative: 2.5% glutaraldehyde in 50 mM Na-cacodylate buffer (pH 7.4) containing 50 mM KCl, 2.6 mM $MgCl_2$, 2.6 mM $CaCl_2$ and 2% sucrose) to the cell culture medium (1:1) for 5 min at RT in 12 wells plates. Fixative was removed and replaced by 1x fixative for 2 h at RT. Plates were plunged in 6% formaldehyde for inactivation for 30 min at RT before being transported outside the BSL3 area. Fixative was exchanged again with 1x EM fixative and the samples were stored at 4°C until further processing. Prior to embedding cells were rinsed 6 times with 100 mM Na-cacodylate for 10 min each. Subsequently, cells were post-fixed with osmium-ferricyanide (1% OsO_4, 1.5% $K_3Fe(III)(CN)_6$, 0.065 M Na-cacodylate buffer) for 2 h at 4°C in the dark. Further processing was done in the microwave. Cells were washed five times with dH_2O for 1 min each, stained four times with 1% uranyl acetate in dH_2O for 2 min each, rinsed three times with dH_2O for 1 min. Dehydration with an ethanol series (50%, 70%, 90% and 4x 100%) was then performed for 40 s each on ice in the microwave. Cells were infiltrated in Epon 812 resin with increasing percentages of this resin in ethanol (10%, 30%, 50%, 70%, 90% and 2x 100%) for 3 min each in the microwave. The coverslips with the cells facing down were placed on a BEEM capsule filled with Epon 812 resin. Beem capsule and coverslip were turned upside down and polymerized at 60°C. After one day the glass coverslips were removed from the blocks that were incubated for 2 more days at 60°C. Ultrathin sections (70 nm) were obtained with a UC7 Leica conventional ultramicrotome with a diamond knife (Diatome) and collected on slot grids. Grids were post-stained with Uranyl acetate and lead citrate. Sections were analyzed with a JEOL 2010 plus transmission electron microscope equipped with a Matataki sCMOS camera.

Electron Tomography (Sample Acquisition, Reconstruction and Rendering)

Sections of 300 nm (Calu-3 cells, MOI = 0.5, 24 h after infection) and 200 nm (all other conditions) thickness processed as described for TEM, were collected on Formvar-coated slot grids. After post-staining, screening images were acquired at 1000 × and 3000 × magnification at points evenly distributed across one section. This was done using advanced SerialEM functionality at a JEM 2100 Plus electron microscope (JEOL Ltd., Akishima, Japan) equipped with a Jeol Matataki sCMOS camera (Schorb et al., 2019). The higher magnification images were manually screened for target features. After transferring and registering the grids to a TF30 microscope (Thermo Fisher Scientific, Waltham, MA, USA), equipped with a Gatan OneView (Gatan, Inc. Pleasanton, US), precise target positions were manually selected within the previously defined regions and acquired by dual axis tomography (−60° to +60° per axis; increment: 1°) at 15,500 × magnification (1.55 nm/px). The tilt series were reconstructed on a high-performance computer cluster using IMOD's automated batch reconstruction (Kremer et al., 1996; Mastronarde, 2005; Mastronarde and Held, 2017). Selected tomograms or parts thereof were manually segmented in Amira-Avizo software Version 2020.1, using the magic wand and the brush segmentation tools. Volume rendering and animations were computed with Amira and post-processed in ImageJ (Schindelin et al., 2012; Schneider et al., 2012).

Sample Preparation for FIB-SEM

Calu-3 cells were grown on 35-mm-diameter MatTek dishes with glass bottom and were prepared (infection and fixation) as described above for TEM. Extra post-staining steps were performed (the so called OTO post-staining). Cells were post-fixed with osmium-ferricyanide (1% OsO_4, 1.5% $K_3Fe(III)(CN)_6$, 0.065 M Na-cacodylate buffer) for 2 h at 4°C in the dark. Further processing was done in the microwave. Cells were rinsed five times in dH_2O for 1 min each and treated with 1% thiocarbohydrazide in dH_2O four times for 2 min each. Cells were rinsed three times with dH_2O for 1 min each and stained four times with 2% osmium tetroxide in dH_2O for 2 min each. Cells were rinsed three times with dH_2O for 1 min, stained with 1% Uranyl acetate in dH_2O four times for 2 min each. Dehydration and embedding were done as described for TEM sample preparation except that Durcupan resin was used. Cells were embedded in a thin layer of Durcupan resin covered with a coverslip and polymerized overnight at 60°C. After one day the resin slab was detached from the coverslips, polymerized at 100°C for a few h and at 60°C overnight. The polymerized samples were mounted on SEM stubs.

FIB-SEM

FIB-SEM image acquisition was performed with a Zeiss Crossbeam 540 or a Zeiss Crossbeam 550, using the Atlas5 software (FI-BICs, Carl Zeiss Microscopy). Briefly, a platinum coating was deposited over the cells of interest and autotune marks were etched and used for post-acquisition image alignment. The imaging surface was exposed by FIB-milling of a 25-30 μm deep trench. FIB slicing during the run was obtained at 700 pA/1.5 nA. All datasets were acquired at 1.5 kV and 700 pA current using an energy-selective back-scattered electron detector (ESB). The cells were acquired at 8x8x8 nm (or 5 × 5 × 5 nm) voxel size.

Alignment of image slices was performed by a workflow based on Alignment to Median Smoothed Template (AMST) (Hennies et al., 2020). Pre-alignment was performed by linear stack alignment with SIFT (Lowe, 2004) and subsequent template matching on the autotune marks. The displacements obtained by template matching were smoothed along the z-direction for more robustness and applied to the SIFT aligned data stack. Subsequent AMST yielded the final aligned datasets.

Segmentation of DMVs, ER and mitochondria was performed in semi- and fully automated manner in an original workflow that will be detailed elsewhere. The semi-automated workflow, based on supervoxel merging using Paintera (https://github.com/saalfeldlab/paintera) (Hanslovsky et al., 2020), was used to obtain the necessary ground truth for the automated workflow. The automated segmentation is an adaptation of the multicut pipeline (Beier et al., 2017), optimized for the segmentation of cellular organelles. Masks for the target cells were obtained using Microscopy Image Browser MIB (Belevich et al., 2016) by annotation of selected slices and interpolation. Nuclei were segmented in MIB using the graph-cut approach. Golgi stacks were segmented using MIB by annotation of selected slices with interpolation. Subsequent adaptive thresholding (Otsu, 1979) within the annotated area, individually for each Golgi stack, yielded the final segmentation. For the mock cell, we annotated ∼20 stacks and used a U-Net (Çiçek et al., 2016) to scale up to the full cell. 3D renderings of above described segmentations were performed using Drishti (Limaye, 2012).

Electron Microscopy Dataset Visualization through MoBIE

The Fiji plugin MoBIE can be used to visualize all the tomographic datasets (Vergara et al., 2020). Instructions for the plugin download and installation can be found at the following link: https://github.com/mobie/mobie-viewer-fiji. To visualize the electron microscopy datasets, the link to the datasets (https://github.com/mobie/covid-tomo-datasets for the tomograms and https://github.com/mobie/covid-em-datasets for the FIB-SEM datasets) should be inserted into the "Project location" of Fiji. Additional information how to access and used the datasets is provided in Table S1.

STATISTICAL ANALYSIS AND QUANTIFICATION

All statistical analyses were performed with the GraphPad Prism 7.04 software package (La Jolla, CA, USA). Datasets were considered significantly different if the p value was less than 0.05. For each experiment, the performed statistical analysis and the sample sizes are given in the respective figure legend.